Title
Chemosensory Ca2+ Dynamics Correlate with Diverse Behavioral Phenotypes in Human Sperm*

Journal
Journal of Biological Chemistry, 286(19)

ISSN
0021-9258

Authors
Veitinger, Thomas
Riffell, Jeffrey R
Veitinger, Sophie
et al.

Publication Date
2011-05-01

DOI
10.1074/jbc.m110.211524

THE JOURNAL OF BIOLOGICAL CHEMISTRY VOL. 286, NO. 19, pp. 17311–17325, May 13, 2011

Chemosensory Ca^{2+} Dynamics Correlate with Diverse Behavioral Phenotypes in Human Sperm*[S]

Received for publication, December 11, 2010, and in revised form, March 18, 2011 Published, JBC Papers in Press, March 21, 2011, DOI 10.1074/jbc.M110.211524

Thomas Veitinger[‡§1], Jeffrey R. Riffell[¶1], Sophie Veitinger[‡§1], Jaclyn M. Nascimento[‖], Annika Triller[§], Charlie Chandsawangbhuwana[**], Katlen Schwane[§], Andreas Geerts[‡‡], Frank Wunder[‡‡], Michael W. Berns[§§], Eva M. Neuhaus[¶¶], Richard K. Zimmer[‖‖2], Marc Spehr[‡2,3], and Hanns Hatt[§2]**

*From the [‡]Department of Chemosensation, Institute for Biology II, Rheinisch-Westfaelische Technische Hochschule-Aachen University, 52074 Aachen, Germany, the [§]Department of Cellular Physiology, Ruhr-University, 44780 Bochum, Germany, the [¶]Department of Neuroscience, University of Arizona, Tucson, Arizona 85721, the Departments of [‖]Electrical and Computer Engineering and **Department of Bioengineering, University of California, San Diego, La Jolla, California 92093-0412, the [‡‡]Bayer Schering Pharma AG Pharma Research Center, 42096 Wuppertal, Germany, the [§§]Beckman Laser Institute, University of California, Irvine, California, the [¶¶]Charité-NeuroScience Research Center, 10117 Berlin, Germany, and the [‖‖]Department of Ecology and Evolutionary Biology, Neuroscience Program, and Brain Research Institute, UCLA, Los Angeles, California 90095-1606*

In the female reproductive tract, mammalian sperm undergo a regulated sequence of prefusion changes that "prime" sperm for fertilization. Among the least understood of these complex processes are the molecular mechanisms that underlie sperm guidance by environmental chemical cues. A "hard-wired" Ca^{2+} signaling strategy that orchestrates specific motility patterns according to given functional requirements is an emerging concept for regulation of sperm swimming behavior. The molecular players involved, the spatiotemporal characteristics of such motility-associated Ca^{2+} dynamics, and the relation between a distinct Ca^{2+} signaling pattern and a behavioral sperm phenotype, however, remain largely unclear. Here, we report the functional characterization of two human sperm chemoreceptors. Using complementary molecular, physiological, and behavioral approaches, we comparatively describe sperm Ca^{2+} responses to specific agonists of these novel receptors and bourgeonal, a known sperm chemoattractant. We further show that individual receptor activation induces specific Ca^{2+} signaling patterns with unique spatiotemporal dynamics. These distinct Ca^{2+} dynamics are correlated to a set of stimulus-specific stereotyped behavioral responses that could play vital roles during various stages of prefusion sperm-egg chemical communication.

On their journey to locate the oocyte, navigating mammalian sperm depend on both chemical (1) and physical (2, 3) cues to regulate flagellar motion, switch flagellar beat modes, and, thus, direct their movement. How such environmental signals are detected and translated into changes in motility, however, remains largely unknown.

Sperm acquire motility upon vaginal deposition (4). This initial swimming behavior is referred to as activated motility and characterized by a relatively low amplitude/high frequency sinusoidal flagellar motion (5). Motile sperm that pass the cervical mucus barrier must locate and enter the oviduct. Only a fraction of sperm present in the uterus (~10% in humans (6)) accomplishes this task. Within the oviductal isthmus, sperm frequently attach to the highly convoluted epithelial surface (3, 7, 8), forming a sperm reservoir in close proximity to the fertilization site. Upon ovulation, capacitated sperm that adopt a hyperactivated state (*i.e.* displaying asymmetrical and relatively high amplitude/low frequency flagellar beating) (4), generate sufficient propulsion force to detach from the epithelium, enter the ampulla, and eventually penetrate the cumulus and zona pellucida surrounding the egg (9).

Given the small fraction of sperm that reaches the oviduct, a "competitive race" scenario has fallen out of favor in recent years. Instead, effective sperm guidance mechanisms are required to assure a synchronized arrival and encounter of both gametes at the fertilization site (1). Current models propose a complex multistep process of sperm navigation along thermal (2) and chemical (10) gradients. Accordingly, chemical guidance cues are secreted by both the oocyte and the surrounding cumulus cells after ovulation (11). In addition to these chemoattractants, further unidentified chemosignals may participate in other prefusion processes that prime sperm for fertilization (12).

In contrast to the far more advanced knowledge about marine invertebrate sperm chemotaxis (13–15), the ligands and receptors involved in mammalian sperm-oocyte communication are largely unknown (1, 3, 7). In this context, we and others (16–20) recently proposed a functional role of sperm chemosensory receptors that, based on sequence homology analysis, are members of the G protein-coupled receptor superfamily of

* This work was supported, in whole or in part, by National Institutes of Health Grant 2 K12 GM000708-06 (to J. R. R.). This work was also supported by grants from the Volkswagen Foundation (to M. S.), the Deutsche Forschungsgemeinschaft (to H. H. and M. S.), National Science Foundation Grant IOS 08-20645 (to R. K. Z.), a Graduate Research Fellowship (to C. C.), the Heinrich und Alma Vogelsang-Foundation (to K. S.), the United States Department of Defense (to C. C.) (National Defense Science and Engineering Graduate Fellowship), the Beckman Laser Institute Inc. Foundation (to M. W. B. and J. M. N.), and the UCLA Council on Research (to R. K. Z.).

[S] The on-line version of this article (available at http://www.jbc.org) contains supplemental Table S1 and Figs. S1–S5.

[1] These authors contributed equally to this work.

[2] These authors contributed equally to this work.

[3] A Lichtenberg Professor of the Volkswagen Foundation. To whom correspondence should be addressed: LuF Chemosensorik, Institute for Biology II, RWTH-Aachen University, 52074 Aachen, Germany. Fax: 49-241-8022802; E-mail: m.spehr@sensorik.rwth-aachen.de.

odorant receptor (OR)[4] proteins (21, 22). Many laboratories have consistently reported OR expression in mammalian male reproductive tissues, pre- and postmeiotic germ cells, and mature spermatozoa (16–19, 23–36). In recent microarray surveys, up to 83 different human OR genes were found expressed in testes (28, 36), and several of these testicular ORs appear to have evolved under stronger evolutionary constraint than OR genes expressed exclusively in the olfactory epithelium (36, 37). So far, however, only two such receptors (OR1D2 (17) in humans and Olfr16 (19) in mice, respectively) have been attributed physiological functions as mediators of sperm chemotaxis. OR1D2 is activated *in vitro* by the synthetic odor molecule bourgeonal but antagonized by the unrelated aldehyde undecanal (17, 38–40). When human sperm are exposed to an ascending bourgeonal gradient, a fraction of cells displays robust chemotactic behavior (1, 41), which is abolished by undecanal (16, 17). Analogous to peptide-mediated sperm chemotaxis in marine invertebrates (15), bourgeonal-triggered cytosolic Ca^{2+} signals are believed to control changes in flagellar beating that underlie chemotactic swimming behavior in human sperm.

Playing a pivotal role in the vast majority of cellular signaling processes, the cytosolic Ca^{2+} concentration is subject to tight spatiotemporal control (42, 43) in both somatic and germ cells. In sperm, the restricted cytoplasmic volume and highly polarized morphology pose a unique challenge for the cell to orchestrate discrete Ca^{2+}-sensitive responses and maintain Ca^{2+} signaling specificity (3, 44). In addition, developing sperm shed most intracellular membranous organelles during spermiogenesis, retaining only the acrosome, the redundant nuclear envelope, and the mitochondria as potential Ca^{2+} stores (45). Thus, some components of the somatic cell Ca^{2+} signaling "tool kit" are not available to control Ca^{2+} dynamics and coordinate the flagellar waveform. However, sperm appear to employ a "hardwired" Ca^{2+} signaling strategy in which a given stimulus generates a distinct Ca^{2+} signal in separate microdomains and little if any input integration occurs (44). This way, specific Ca^{2+}-regulated motility patterns (*e.g.* chemotactic turns, hyperactivation, etc.) are initiated according to the cell's functional requirements. The spatiotemporal characteristics of such motility-associated Ca^{2+} dynamics in human sperm, however, remain unclear.

Here, we report functional characterization of two human sperm chemoreceptors. We identify receptor-specific agonists and comparatively describe physiological Ca^{2+} responses in sperm to these novel stimuli and bourgeonal, a known sperm chemoattractant. We further show that individual receptor activation induces Ca^{2+} signals with unique spatiotemporal dynamics. These distinct Ca^{2+} mobilization patterns are correlated to a set of stimulus-specific stereotyped behavioral responses that could mediate chemical communication during various prefusion stages.

[4] The abbreviations used are: OR, odorant receptor; CAVMA, computer-assisted video motion analysis; HTF, human tubal fluid; RATTS, real-time automated tracking and trapping system.

EXPERIMENTAL PROCEDURES

Reverse Transcription-PCR

Total RNA from pooled human testis samples was isolated using TRIzol reagent according to the manufacturer's instructions (Invitrogen). After DNase I digestion, poly(A)$^+$ mRNA bound to oligo(dT)-coated paramagnetic particles (Dynal, Oslo, Norway) was isolated, and cDNA was generated using Moloney murine leukemia virus reverse transcriptase (Invitrogen) and oligo(dT)$_{12-18}$ primer. PCR amplification was performed during 30 thermal cycles (94 °C, 1 min; 60 °C, 1 min; 72 °C, 1 min) with specific primer pairs corresponding to the following (genes and GenBank™ accession numbers listed): *OR1D2* (NM_002548), *OR7A5* (NM_017506), *OR4D1* (NM_012374), *OR5D16* (NM_001005496), *OR2M4* (NM_017504), β-actin (NM_001101), *GAPDH* (NM_002046), and *PGK1* (NM_000291). Individual PCR products were separated and visualized on an agarose gel via ethidium bromide staining, and product identity was confirmed by sequencing. The absence of detectable PCR products after reverse transcription was omitted controlled for potential contamination.

Quantitative Real-time RT-PCR Analysis

Quantitative TaqMan RT-PCR analysis was performed using the Applied Biosystems PRISM 7900 sequence detection system. Human tissue mRNA probes were obtained from Ambion, Inc. (Austin, TX), BioChain Institute, Inc. (Hayward, CA), Clontech Laboratories (Mountain View, CA), and Stratagene (La Jolla, CA). DNase I digestion was performed to remove residual genomic DNA, and mRNAs were reverse transcribed using random hexamer primers. Specific odorant receptor probes were carefully designed, and comparable probe efficiencies were assured by amplification of genomic DNA. Results were normalized to β-actin controls, and relative expression (arbitrary units) was calculated according to the following formula: relative expression $= 2^{(18 - (Ct(\text{probe}) - Ct(\text{actin})))}$. The threshold parameter *Ct* is defined as the cycle number at which the amplification plot passes a fixed threshold above base line. The primers and fluorescent probes used are described in supplemental Table S1.

Recombinant Odorant Receptor Expression

Human embryonic kidney 293 (HEK293) cells were cultured in DMEM (100 units/ml penicillin, 100 μg/ml streptomycin) supplemented with 10% fetal calf serum as described previously (17, 46). Transfection of semiconfluent HEK293 cells with full-length PCR products cloned into pcDNA3 vectors (Invitrogen) was conducted using the calcium phosphate precipitation technique, and transfection efficiency was monitored as described (17, 38). In some experiments, we coexpressed RTP1, RTP2, and REEP1 to promote functional cell surface expression (47). Ca^{2+} imaging experiments were performed 48–72 h after transfection.

Sperm Preparation

Motility Analysis Using Computer-assisted Video Motion Analysis (CAVMA)—Frozen semen samples of healthy donors were prepared for bioassays using a two-wash protocol (48), according to World Health Organization guidelines. After bringing suspensions to 37 °C over 10 min, each sperm sample was adjusted to 10^6 cells/ml, placed in HEPES-buffered human tubal fluid (HTF; Irvine Scientific, Santa Ana, CA), and incubated at 37 °C in a 5% CO_2 atmosphere for 30 min.

Motility Analysis Using Laser Tweezers—Frozen human semen samples from several healthy donors were prepared for bioassays as described above. Sperm was suspended in HEPES-buffered HTF (osmolarity ~280 mosmol/liter, pH 7.4). A dilution of ~30,000 sperm/ml was transferred into a Rose tissue culture chamber and mounted on a microscope stage. The sample was kept at 37 °C using an air curtain incubator (ASI 400 Air Stream Incubator, NEVTEK, Burnsville, VA). A thermocouple was attached to the Rose chamber to ensure temperature stability.

Ca^{2+} Imaging Analysis—Fresh human sperm was collected from young healthy donors who gave informed consent ($n \geq 4$; 25–41 years). Percoll density gradient centrifugation was performed after liquefaction (30 min at 35.5 °C) as described previously (16). In brief, liquefied semen was overlaid on a two-layer Percoll (Amersham Biosciences, Freiburg, Germany) density gradient consisting of 80 and 55% isotonic Percoll in Ham's F-10 medium (Invitrogen). After a 30-min centrifugation (500 × *g*, room temperature) the supernatant was discarded, and the pellet was resuspended in 5 ml of standard Ringer's solution containing 145 mM NaCl, 5 mM KCl, 1 mM $CaCl_2$, 1 mM $MgCl_2$, 10 mM Hepes, pH 7.4 (osmolarity = 300 mosmol/liter). After subsequent centrifugation (500 × *g*, 15 min, room temperature), the pellet was resuspended in 2 ml of Ringer's solution containing 7.5 μM fura-2/AM (Molecular Probes, Leiden, The Netherlands). For dye loading, cells were transferred to concanavalin A-coated 35-mm glass bottom dishes, protected from light, and incubated for 45 min. Fura-2-loaded, adhered sperm were washed twice with Ringer's solution to remove extracellular fura-2/AM.

Single Cell Ca^{2+} Imaging Analysis

Glass-bottom dishes, containing either human sperm adhered to concanavalin A coating or cultured HEK293 cells (loaded with fura-2/AM; 3 μM; 30 min), were transferred to the stage of an inverted microscope equipped for ratiometric live cell imaging (Olympus IX71) with a 150-watt xenon arc lamp, a motorized fast change filter wheel illumination system (MT20, Olympus) for multiwavelength excitation, a 12-bit 1376 × 1032-pixel charge-coupled device (CCD) camera (F-View II, Olympus), and cellR̂ imaging software (Olympus). Cells in a randomly selected field of view were viewed at ×60 magnification using an oil immersion objective (UPLSAPO; numerical aperture = 1.35; Olympus) and illuminated sequentially at 340 and 380 nm at variable cycle times (sperm, 200 or 1000 ms, respectively; HEK293, 1000 ms). The average pixel intensity within user-selected regions of interest was digitized and stored on a PC. Ca^{2+}-dependent fluorescence signals at 510 nm were calculated as the F_{340}/F_{380} intensity ratio. Stimuli were applied using a custom-made pressure-driven multibarrel perfusion system that allows for instantaneous solution change and focal application. Single sperm imaging experiments were repeated multiple times using cells from at least four different donors. In recombinant OR characterization experiments that tested for a specific stimulus mixture or a single agonist, Ca^{2+} imaging measurements were performed repeatedly ($n \geq 30$) using cells from at least three independent transfections (in parallel to untransfected controls).

Sperm Population Ca^{2+} Imaging

Population Ca^{2+} imaging experiments were performed as previously described (17). Briefly, diluted fura-2-loaded sperm suspension (cell density adjusted to $E_{260} = 0.035$) were transferred to 96-well plates (150 μl/well). After stimulation in the absence and presence of different agents, individual wells were illuminated (1 s) at 330 ± 20 nm/380 ± 10 nm, and Ca^{2+}-dependent ratiometric (F_{340}/F_{380}) fluorescence signals at 515 ± 10 nm were detected using a Fusion-α Universal Multiplate Analyzer (PerkinElmer Life Sciences).

Microcapillary Bioassays

Microcapillary bioassays were performed as described previously (6, 17) to distinguish between mechanisms of chemotaxis, chemokinesis, and other processes that might cause sperm accumulation (1). Briefly, two opposing wells containing fresh sperm suspensions (10^6 cells/ml) were connected by a 6-μl microcapillary tube. Sperm were exposed in parallel experiments to (*a*) an ascending chemical concentration gradient (capillaries containing stimuli, wells filled with HTF), (*b*) a uniform concentration (stimulus present in both capillaries and wells), or (*c*) a descending gradient (wells filled with stimuli, capillaries containing HTF). At least four replicate trials were performed for every test, using sperm from different human donors. After incubation (60 min, 37 °C), the contents of each capillary were transferred to toxoplasmosis slides, heat-fixed, and stained with 0.1% acridine orange. During trials, O_2 microelectrode measurements showed no change in oxygen levels inside and outside of the capillaries. Cell counts were determined using an inverted phase-contrast microscope (Olympus BH2).

CAVMA

Microcapillary bioassays were combined with CAVMA as described previously (17, 49) to determine behavioral/motility effects induced by exposure to odor gradients. For each stimulus concentration (10^{-8} to 10^{-5} M), four replicate trials were performed in a 4 (concentration) × 6 (stimuli) factor design. Sperm from different donors were used in each trial. Swimming speeds and directions of individual cells were videotaped over 15 s, beginning 10–15 min after the start of each microcapillary bioassay. Fluid dynamic theory predicts that the concentration gradient within 300 μm of the capillary tip should reach a steady state within ~10 min. In addition, the presence of a steep, ascending gradient was confirmed by quantifying fluorescent marker release (rhodamine) through fluorescence imaging. Rhodamine concentration (*a*) remained highest at the tip, decreasing as approximately the three-halves power of time and (*b*) decreased geometrically as a function of 1/distance from the tip (consistent with mass transport via molecular diffusion). Using non-motile sperm as tracers for flow visualization, fluid motion (due to convection, flow from the pipette, and mixing) was found to be insignificant (<5 μm/s) when compared with swimming speeds of live cells (17). Sperm images were recorded on magnetic tape as described (49), using a cooled CCD camera (6415-2000, Cohu (San Diego, CA)) mounted on an inverted light microscope (Olympus IX70, Melville, NY) at ×90 magnification. A region within 300 μm of the microcapillary tip was monitored at ∼100 μm depth of field. According to fluid dynamic theory, drag forces show effects on flagellar motion within a distance of ∼10 sperm body lengths from a microscope slide surface. To avoid potential artifacts, we assayed sperm motility in response to chemical stimuli at ∼2 mm (*i.e.* ∼35 sperm body lengths) from the nearest chamber wall. Images were digitized at 30-Hz frame rates and processed using a CAVMA system (VP320; Motion Analysis Corp., Santa Rosa, CA) and custom software interfaced with a Sun SPARC2 computer work station (50). To avoid parallax, we discarded paths in which apparent sperm head size changed between frames by more than 20%. Swimming speed was determined on a frame-by-frame basis and averaged over each path. The angle of sperm orientation (θ) was measured with respect to an origin (0°), defined as the shortest tangent between each cell and the capillary tip. Using circular statistics, a mean vector (r) was calculated to describe the average direction of movement of a cell population (vector length = 1 indicates that all cells swim in a single, common direction; vector length = 0 indicates random motion).

Flagellar Beating Analysis

Beat frequency of an individual sperm flagellum was determined as an adjunct to analysis of swimming behavior (see above). Microcapillary assays were repeated for each test or control treatment (at 37 °C and 5% CO_2 atmosphere). Sperm, however, were exposed only to ascending concentration gradients. After a gradient had been established (10 min), motile sperm were photographed at 30 Hz as described. Beat patterns were determined for 10–24 cells/test or control, respectively. A random sampling of cells was used in each analysis, with the following caveats: (*a*) cells were motile; (*b*) they remained within the focal plane of the camera for one continuous second or longer (*i.e.* 30 images or more); and (*c*) they were positioned less than 150 μm from the capillary tip. National Institutes of Health ImageJ software was used to calculate the average beat frequency of a sperm's flagellum as the reciprocal of total time elapsed over three complete beat cycles, divided by 3. This calculation gave highly reproducible results.

Acrosome Reaction Assay

The ability of sperm to undergo the acrosome reaction was determined from an independent series of microcapillary assays. 4-μl samples of cells residing either in wells or in capillaries were collected after a 1-h incubation (37 °C) in ascending gradients of bourgeonal, Myrac, or PI-23472 (*versus* HTF controls; 5 replicates/treatment/control). Each sample was split into equal volumes (2 μl) and treated as follows. The first volume was cooled on ice for 10 min, added to 95% methanol (2 μl) for 30 s, and then reacted for 30 min with 5 μl of the acrosomal marker fluorescein isothiocyanate-conjugated *Pisum sativum* agglutinin (FITC-PSA; 1 mg/ml). After wash (HTF), the sample was centrifuged (300 × *g*, 5 min), transferred to toxoplasmosis slides, and air-dried. Using fluorescence microscopy (×1000; Olympus BX40), the percentage of cells that had spontaneously undergone the acrosome reaction was determined for the first 200 sperm encountered. Reacted sperm retained a unique equatorial stain, as opposed to exhibiting uniform fluorescence across the entire head. In the second volume, cells were challenged for 30 min with 5 μl of phorbol 12-myristate 13-acetate (5 μM) prior to incubating with FITC-PSA and counting. Inducing the acrosome reaction, phorbol 12-myristate 13-acetate affects only sperm in a capacitated state. The combined percentage of sperm exhibiting either spontaneous or induced acrosome reactions indicates the total population of cells capable of binding to and penetrating the zona pellucida (51).

Motility Analysis Using Laser Tweezers

The laser tweezers optical design, hardware, sperm tracking software, experimental procedure, and analysis of sperm have been described in detail elsewhere (52, 53). Briefly, a single point gradient trap was generated using an Nd:YVO_4 continuous wave 1064-nm wavelength laser (BL-106C, Spectra Physics, Mountain View, CA), coupled to a Zeiss Axiovert S100 microscope equipped with a phase III, oil immersion objective (×40 magnification; numerical aperture = 1.3). Phase-contrast images of swimming sperm were acquired at a 40-Hz frame rate using a CCD camera (Cohu 7800). Individual sperm were randomly selected and automatically tracked and trapped using the real-time automated tracking and trapping system (RATTS). In an operational mode analogous to conventional computer-assisted sperm analysis, the swimming speed (curvilinear velocity (μm/s)) was calculated based on the pixel coordinates (x/y) of the sperm's swimming trajectory. Once a cell was automatically trapped by RATTS, the laser power was continually attenuated by rotating a linear polarizer set in a stepper-motor-controlled rotating mount (PR50PP, Newport Corp., Irvine, CA). The laser power at which the sperm was capable of escaping the trap was recorded (escape power, P_{esc} (milliwatts)) and converted to swimming force in piconewtons by the equation, $F = n_1QP/c$ (54). The odorant stimulus solution was delivered through 1⁄32-inch inner diameter Tygon tubing connected to a 1½-inch 21-gauge needle shaft. After a specimen was loaded onto the microscope, the needle was inserted through the silicon gasket and positioned to the center of the chamber. Immediately after insertion, 10 μl of the odorant solution were injected, and calculations of the curvilinear velocity and escape laser power began. Only sperm in close vicinity to the needle exit were analyzed. This analysis lasted for 5 min. Odorant and non-odorant chambers were alternated during the span of the experiment.

ELISA-based Cyclic Nucleotide Assays

For quantitative determination of intracellular cAMP/cGMP, a commercial kit was used according to the manufacturer's instructions (Enzo Life Sciences, Loerrach, Germany). Briefly, pooled sperm samples (4–5 donors) were prepared as described above, and cell density was adjusted to $\sim 4 \times 10^8$ cells/ml (20 μl). Equal volumes of stimulus solution (IBMX (200 μM) and either bourgeonal, Myrac, PI-23472 (10 μM each),

$NaHCO_3$ (30 mM), or SNP (1 M)) were added. After 30 s, reactions were stopped. Desiccated lysates (5 h; 37 °C) were reconstituted in 0.1 M HCl, and 100-μl samples were transferred to a microtiter plate. cAMP/cGMP concentrations were measured according to the manufacturer's instructions with the following changes. To exclude differences in antibody binding efficiency, all samples and standards were adjusted to identical ionic conditions. For each tested condition and standard, three replicate experiments were performed, and results were averaged.

Statistical Analysis

All data were obtained from sperm samples of at least three (usually five or more) different donors. If not stated otherwise, results are presented as means ± S.E., and statistical analyses were performed using paired or unpaired Student's *t* tests (as dictated by data distribution and experimental design). To determine if cell movement within a chemical gradient was non-random during CAVMA, each mean direction was compared with a uniform circular distribution using Rayleigh's test. Data from microcapillary bioassays were analyzed statistically by a two-way ANOVA using stimulus concentration and gradient type as factors, followed by *post hoc* Scheffé tests (17, 49). The curvilinear velocity and escape laser power distributions resulting from the experiments testing the effects of the three odorants were statistically compared using the non-parametric Wilcoxon rank sum test (based on 5% significance). The distributions are displayed graphically in *box plot* form (Fig. 6*C*). Each *box plot* displays the following parameters for a given distribution: (*a*) median (*center line* of *box*), (*b*) lower and upper quartile values (*bottom* and *top line* of *box*, respectively), (*c*) the range of the data (*dashed lines* extending from the *top* and *bottom* of *box*), and (*d*) the data points lying outside 3 times the interquartile range. *Notches* in the *box* represent an estimate of the uncertainty about the median value. If notches on the box plots of two groups do not overlap, it can be concluded with 95% confidence that the two medians differ.

Chemicals and Reagents

Unless stated otherwise, all chemicals and reagents were obtained from Sigma-Aldrich (Schnelldorf, Germany).

RESULTS

Distinct Agonist Profiles of Three Human Testicular Chemoreceptors—To understand the functional link between chemoreceptor activation, Ca^{2+} signaling, and swimming behavior in human sperm, we aimed to identify stimuli that specifically activate orphan testicular ORs. We concentrated on two distinct receptors, *OR4D1* and *OR7A5*, which had previously been found expressed at high levels in human testicular tissue and/or fertile human sperm by various groups (24, 25, 32, 35). First, we confirmed testicular expression of *OR4D1* and *OR7A5* by RT-PCR (Fig. 1*A*, *inset*) using *OR1D2* as a positive control (17). We next examined whether this expression pattern is tissue-specific or a result of "leaky" and therefore tissue-independent low level OR transcription. In a series of quantitative real-time PCR experiments, we comparatively surveyed relative mRNA expression levels of *OR4D1*, *OR7A5*, and *OR1D2* in nine different human tissues (Fig. 1*A*). Our results indicate no (or negligible) OR gene transcription in heart, lung, liver, stomach, aorta, brain, skeletal muscle, and prostate. By contrast, all three receptors were expressed at significant levels in testicular tissue samples.

Analogous to an experimental protocol we previously used successfully to deorphanize human ORs (17, 55–57), we cloned both *OR4D1* and *OR7A5* and expressed individual recombinant receptors in HEK293 cells (Fig. 1, *B* and C) (17, 57). Fura-2-loaded HEK293 cells were challenged with a complex library of more than 100 different low molecular weight chemicals (generously provided by Johannes Panten, Symrise AG, Holzminden, Germany). Those cells that functionally expressed either OR7A5 or OR4D1 displayed robust Ca^{2+} signals when exposed to the stimulus mixture (data not shown), whereas stimulus-dependent Ca^{2+} responses were never observed in nontransfected cells. We then divided the stimulus into different submixtures (17, 55–57) and determined the specific fraction activating either OR7A5 or OR4D1, respectively. After several such cycles, we identified two receptor-ligand pairs. OR7A5 is activated by 4-(4-methyl-3-pentenyl)cyclohex-3-ene-1-carboxaldehyde (Myrac aldehyde) (Fig. 1*B*), whereas OR4D1 responds to 1-(3-(2,2,3-trimethyl-cyclopent-3-enyl)-cyclohex-3-enyl)-ethanone, a compound currently referred to as PI-23472 (Fig. 1*C*). When sequentially challenged with bourgeonal, Myrac, and PI-23472, each recombinant receptor (OR1D2, OR7A5, and OR4D1) selectively responds to its described ligand (Fig. 1, *B* and C, and supplemental Fig. S1*A*). Moreover, antagonistic properties of undecanal were only observed in combination with activation of OR1D2 (16, 17) (supplemental Fig. S1). Consistent with previous reports about other ORs (22, 58), OR4D1 and OR7A5 appear to be rather broadly tuned to a spectrum of structurally similar chemicals. More substantial structural modifications, however, render a molecule inactive (Fig. 1, *B* and *C*).

Chemoreceptor Agonists Mediate Ca^{2+} Signals in Human Sperm—Next, we asked whether the same agonists that activate recombinant testicular chemoreceptors also stimulate individual sperm. Brief (10-s) exposure to bourgeonal, Myrac, or PI-23472 triggered Ca^{2+} transients in single cell fluorescence imaging recordings of fura-2-loaded sperm (Fig. 2*A*). As observed for recombinantly expressed receptors (supplemental Fig. S1), undecanal incubation abolished Ca^{2+} responses to bourgeonal but lacked an inhibitory effect on both Myrac- and PI-23472-induced signals. These data suggest that, analogous to OR1D2 activation in sperm (1, 16, 17, 41), Myrac as well as PI-23472 selectively activate sperm chemoreceptors, probably OR7A5 and OR4D1. Because a hallmark of OR expression in olfactory sensory neurons is their monogenic expression according to a one-cell/one-receptor model (22), we investigated whether bourgeonal, Myrac, and PI-23472 activate receptor-specific sperm subpopulations or if an individual cell can be stimulated by all three chemoreceptor agonists. When sequentially applied in random order at interstimulus intervals of ≥60 s, all three stimuli induce repetitive Ca^{2+} responses in the great majority of sperm (Fig. 2, *B* and *D*, and supplemental Fig. S2*A*). We could, however, exclude a nonspecific activation of sperm by chemical cues *per se*. When sperm populations were challenged in plate reader-based Ca^{2+} assays (17) with either

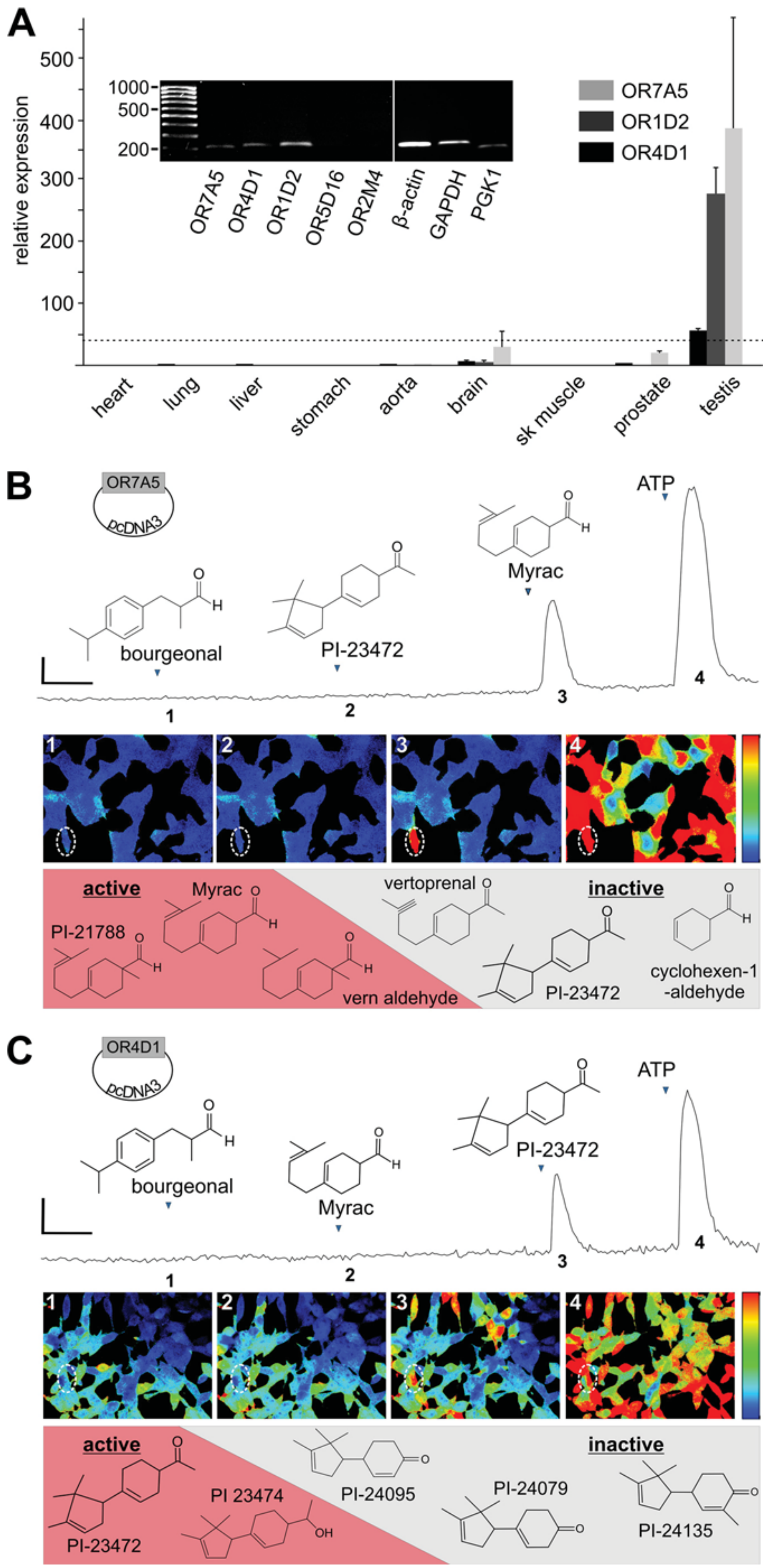
A
relative expression
500
400
300
200
100
1000
500
200
OR7A5
OR4D1
OR1D2
OR5D16
OR2M4
β-actin
GAPDH
PGK1
OR7A5
OR1D2
OR4D1
heart
lung
liver
stomach
aorta
brain
sk muscle
prostate
testis
B
OR7A5
pcDNA3
bourgeonal
PI-23472
Myrac
ATP
1
2
3
4
active
inactive
Myrac
PI-21788
vern aldehyde
vertoprenal
PI-23472
cyclohexen-1
-aldehyde
C
OR4D1
pcDNA3
bourgeonal
Myrac
PI-23472
ATP
1
2
3
4
active
inactive
PI-23472
PI 23474
PI-24095
PI-24079
PI-24135

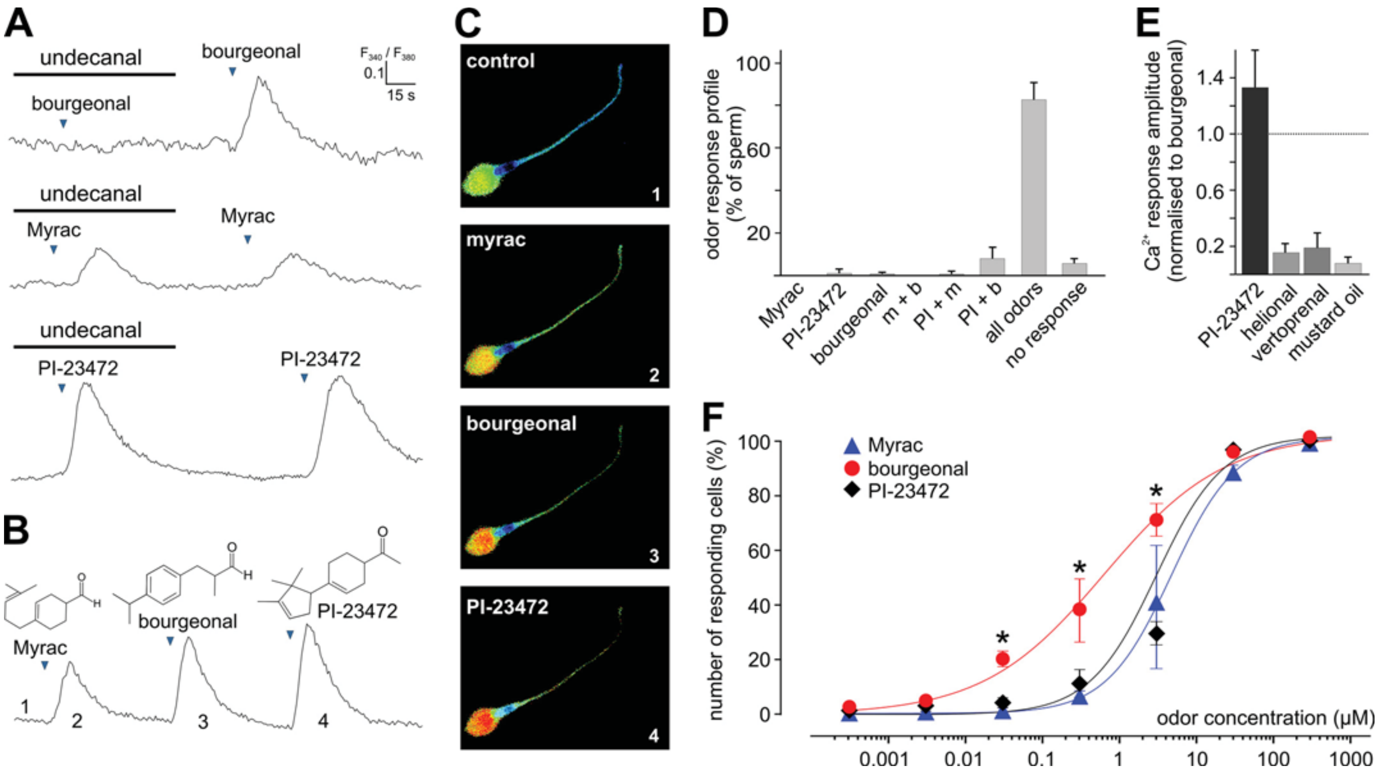

FIGURE 2. **Agonists of OR1D2, OR7A5, and OR4D1 trigger Ca^{2+} transients in human sperm.** *A*, representative Ca^{2+} signals recorded from the head regions of single fura-2-loaded cells. The integrated fluorescence ratio F_{340}/F_{380} is shown as a function of time. Brief focal application of bourgeonal, Myrac, and PI-23472 (50 μM; 10 s) triggers transient increases in Ca^{2+} ($n \geq 41$). As shown for recombinant ORs (supplemental Fig. S1), preincubation with equimolar undecanal (*black horizontal bar*) blocks bourgeonal responses, whereas Myrac and PI-23472 signaling is unaffected ($n = 11$). *B*, a given spermatozoon consecutively responds to ligands that selectively activate different ORs. Shown is a representative original Ca^{2+} recording (F_{340}/F_{380} *versus* time; scaling as shown in *A*) of a single fura-2-loaded cell (depicted in *C*). *Highlighted time points 1–4* correspond to individual *pseudocolor images* (*right*) that illustrate relative changes in Ca^{2+} concentrations (*rainbow 256 color map*; *blue*, low Ca^{2+}; *red*, high Ca^{2+}). *D*, *bar chart* illustrating the relative occurrence of distinct odor sensitivity profiles in individual spermatozoa consecutively challenged with bourgeonal (*b*), Myrac (*m*), and PI-23472 (*PI*) in random sequence (50 μM; 10 s; $n = 311$). *E*, odor specificity of human sperm Ca^{2+} signals as assessed by population response imaging in microtiter plates ($n = 6$). Helional, vertoprenal, and mustard oil essentially fail to activate sperm. Peak ratiometric Ca^{2+} signals (F_{340}/F_{380}) are normalized to bourgeonal-induced response amplitudes (each odor = 50 μM). *F*, normalized quasi-dose-response curves derived from single cell Ca^{2+} imaging experiments ($n = 52$ (bourgeonal), 181 (Myrac), and 309 (PI-23472)). Sigmoid curves were calculated from averaged data points using the Hill equation. Response thresholds are observed in the nanomolar range. Although Myrac and PI-23472 sensitivity are similar with respect to the overall percentage of responding cells, the dose-response curve for bourgeonal stimulation is significantly shifted to lower odor concentrations ($p < 0.05$).

helional (a specific activator of OR3A1 (17, 57, 59, 60)), vertoprenal (a structural analog of Myrac that we found inactive at OR7A5 (Fig. 1*B*)), or mustard oil (a potent TRPA1 channel activator in sensory neurons (61)), Ca^{2+} signals were essentially negligible (Fig. 2*E*). Concentration dependence of bourgeonal, Myrac, and PI-23472 response probability/strength was assessed by calculating normalized quasi-dose-response curves from single cell Ca^{2+} imaging experiments (Fig. 2*F*). As previously reported (17), initial Ca^{2+} responses to bourgeonal were recorded in the low nanomolar range (Fig. 2*F*), whereas both Myrac and PI-23472 response thresholds were right-shifted by approximately 2 orders of magnitude. At stimulus concentrations of ≥30 μM, the maximum percentage of cells was activated by all three stimuli. Independent of the stimulus, responses were critically dependent on the extracellular Ca^{2+} concentration (supplemental Fig. S2, *B* and *C*). Together, human sperm respond to defined ligands of different chemoreceptors with some differences in ligand sensitivity but without any obvious preference for a specific stimulus at saturating concentrations.

What is the nature of the signaling cascade(s) activated downstream receptor-ligand interaction? Our previous results suggested a role of particulate adenylate cyclase and cAMP in OR1D2 signaling (16). In pharmacological single cell assays, we

FIGURE 1. **Expression pattern and response profile of three human testicular odorant receptors.** *A*, testis-specific expression of candidate sperm ORs (*OR1D2*, *OR4D1*, and *OR7A5*) is confirmed by quantitative TaqMan real-time PCR analysis of various human tissues (2–3 different samples/tissue). The *dashed line* indicates relative expression below noise level (cut-off threshold of ≤40). Conventional RT-PCR from human tissue samples (*inset*) substantiates testicular expression of *OR1D2*, *OR4D1*, and *OR7A5*. Two OR genes that had not been attributed ectopic expression before (*OR5D16* and *OR2M4*) served as negative controls. *B* and *C*, characterization of OR7A5 and OR4D1. Receptor activation in response to focal odor application (50 μM; 5 s) is monitored by ratiometric Ca^{2+} signals in fura-2-loaded HEK293 cells (3 μM) transfected with OR-encoding expression vectors (pcDNA3). The original *traces* depict the integrated fluorescence ratio F_{340}/F_{380} of representative odor-sensitive cells (*dashed circles*) as a function of time. *Pseudocolor images* illustrate the relative Ca^{2+} concentration at *time points 1–4* (*rainbow 256 color map*; *blue*, low Ca^{2+}; *red*, high Ca^{2+}). OR7A5 is selectively activated by Myrac, whereas OR4D1 responds to PI-23472. ATP-induced activation of endogenous P2Y receptors (PLC-mediated Ca^{2+} release from internal storage organelles) controls for cell viability. Both ORs accommodate structurally similar ligands (active; *red background color*), whereas more profound changes in chemical structure are not tolerated (inactive; *gray background color*). *Scale bars*, F_{340}/F_{380} = 0.1 (*vertical*); time = 30 s (*horizontal*).

thus tested several inhibitors of adenylate cyclases as well as other signaling proteins (supplemental Fig. S3, *A–G*). Ca^{2+} responses to bourgeonal, Myrac, and PI-23472 were strongly diminished by two adenylate cyclase inhibitors (MDL-12,330A and SQ-22536), whereas KH7, a described blocker of the soluble adenylate cyclase (62), had no effect. A nonspecific effect of SQ-22536 on general Ca^{2+} signal capacity was excluded by stimulation with bicarbonate or elevated extracellular K^+ (supplemental Fig. S3*D*). A battery of agents that target a variety of different signaling molecules showed no significant response inhibition (supplemental Fig. S3*G*). Surprisingly, we did not measure an increase in cAMP upon sperm exposure to bourgeonal, Myrac, or PI-23472 (5 μM) (supplemental Fig. S3*H*); nor did we detect a rise in cGMP levels (supplemental Fig. S3*I*). As positive controls, the soluble adenylate cyclase activator bicarbonate and the NO donor sodium nitroprusside (SNP) triggered a significant increase in cAMP and cGMP, respectively.

Agonist-dependent Ca^{2+} Response Patterns—Ca^{2+} signaling is the common denominator of most physiological processes that occur in sperm, and complex Ca^{2+} dynamics selectively control individual sperm motility patterns (3, 44). Thus, we set out to describe the Ca^{2+} mobilization characteristics in response to bourgeonal, Myrac, and PI-23472, respectively. We used saturating stimulus concentrations (50 μM each) (Fig. 2*F*) to avoid data interpretation errors that could occur when lower agonist concentrations match different stages within the dynamic range of a given receptor/ligand dose-response curve (Fig. 2*F*). For comparative semiquantitative Ca^{2+} measurements both within different subcompartments of the same cell and between different sperm cells, we opted for a fura-2-based ratiometric imaging approach. Using F_{340}/F_{380} measurements corrects for unequal dye loading, bleaching, focal plane shift, dye leakage, and (most important) differences of both optical path length and accessible cytosolic volume (63, 64). We distinguished Ca^{2+} signals in six different sperm compartments (*i.e.* the most anterior area marked by the acrosome cap, the posterior head region, the midpiece, and three different regions of the principal piece (proximal, intermediate, and distal flagellum with respect to the sperm head)) (Fig. 3). For each compartment and stimulus, we analyzed a combination of Ca^{2+} response parameters, including the signal onset, the response amplitude, the rise time (20–80% of amplitude), the rising speed (rise time (s)/amplitude 20–80% (ratio units)), and the Ca^{2+} extrusion kinetics (time constant τ, calculated from monoexponential fits of the Ca^{2+} decay phase).

First, we investigated the origin of the Ca^{2+} signal and its potential propagation through different sperm compartments (Fig. 3, *A* and *B*). For both bourgeonal and PI-23472, significantly increased Ca^{2+} concentrations ($\Delta F_{340}/F_{380} > 2 \times$ S.D.$_{\text{base line}}$) were first observed in the proximal part of the flagellum, whereas Myrac responses originated in the midpiece. For all stimuli, we recorded bilateral Ca^{2+} propagation patterns from the signal origin along a cell's longitudinal axis toward its anterior and posterior end, respectively. With few exceptions, Ca^{2+} signal onsets differed significantly between adjacent compartments (Fig. 3*A*). Maximum delays of 3.16 ± 0.31 s (bourgeonal), 2.48 ± 0.27 s (Myrac), and 2.5 ± 0.39 s (PI-23472) were observed between the first and last detected Ca^{2+} response onset (corresponding to an average longitudinal distance of ~10–30 μm). Moreover, Ca^{2+} signals spread significantly faster toward the sperm head when cells were stimulated with Myrac (Fig. 3, *A* and *D*). These data show that different chemoreceptor agonists elicit Ca^{2+} signals in human sperm that all originate in the proximal area of the principal piece but spread at different speed through the cell, indicating that receptor/ligand-specific mechanisms govern signal propagation.

Next, we examined stimulus-/compartment-dependent Ca^{2+} extrusion kinetics. In a given region, we did not observe stimulus-correlated differences in the Ca^{2+} decay time course (Fig. 3*C*). Extrusion mechanisms, however, established resting Ca^{2+} levels significantly faster in flagellar compartments (4.0–7.6 s) than in the head (19.2–28.7 s) and midpiece (11.0–12.3 s) (Fig. 3, *C* and *F*). Thus, Ca^{2+} removal is receptor/ligand-independent.

When Ca^{2+} response amplitudes were analyzed, PI-23472 induced significantly larger signals than bourgeonal (flagellar regions) or Myrac (all compartments) (Fig. 3, *D* and *E*). Moreover, bourgeonal triggered larger Ca^{2+} signals in the head than observed in Myrac-exposed sperm. Another distinctive parameter of stimulus-dependent Ca^{2+} signals is their individual rising speed. Myrac-mediated Ca^{2+} transients rise significantly slower in all compartments. Differences between bourgeonal and PI-23472 responses are also significant although less pronounced. Plotting both stimulus- and compartment-dependent Ca^{2+} response amplitudes as a function of rising speed, data points group in separated clusters, and stimulus-specific response profiles become apparent (Fig. 3*E*).

Different response patterns became particularly evident when sperm were constantly exposed to a given stimulus for extended periods of time (10 min; 50 μM) (Fig. 4*A*). Both bourgeonal (196 of 209 cells) and PI-23472 (211 of 211 cells) induced a rapidly increasing Ca^{2+} signal, whereas most Myrac responses (83%; 302/341 cells) were characterized by a slow rise in Ca^{2+} (Fig. 4*B*). Compared with bourgeonal responses, PI-23472-dependent peak Ca^{2+} signal amplitudes were strongly elevated (226%; $p < 0.001$), and signal decay was profoundly decelerated. During prolonged exposure to either bourgeonal or Myrac, sperm gradually restored resting Ca^{2+} levels, and subsequently, individual cells either remained quiescent or engaged in slow Ca^{2+} oscillations (79% (bourgeonal) or 78% (Myrac)) (Fig. 4*A*). By contrast, sustained PI-23472 stimulation mediates a constantly elevated Ca^{2+} level that only recovers after cessation of the stimulus. Intriguingly, prolonged prestimulation with PI-23472 (10 min) altered the Myrac-mediated Ca^{2+} response pattern. The predominantly oscillatory behavior changed to a uniform single Ca^{2+} transient ($n = 133$), whereas bourgeonal preincubation did not trigger such an effect ($n = 49$) (Fig. 4, *C* and *D*). Moreover, bourgeonal-induced Ca^{2+} oscillations were unaffected by PI-23472 prestimulation (data not shown). In control experiments, both progesterone (Fig. 4*E*; $n = 120$) and bicarbonate ($n = 74$; data not shown) triggered robust Ca^{2+} signals after PI-23472 pre-exposure, and sperm maintained stable resting Ca^{2+} levels over prolonged time periods when superfused with bath solution (Fig. 4*F*; $n = 30$).

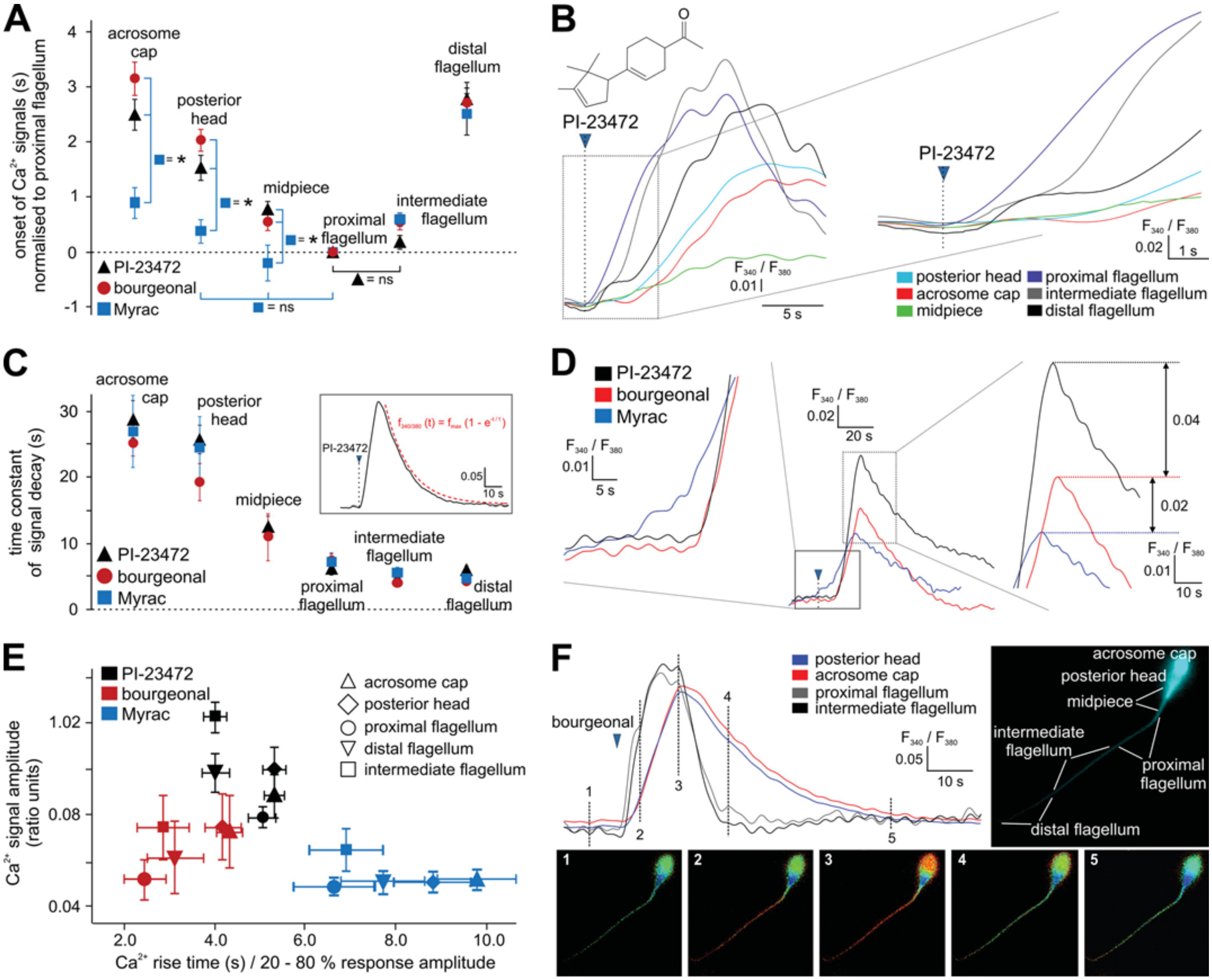

FIGURE 3. **Human sperm display distinct and agonist-specific Ca^{2+} responses.** *A*, heterogeneous distribution of Ca^{2+} signal onsets in different subcellular compartments (as illustrated in *F*). The moment a Ca^{2+} response is detected in the proximal flagellum is set as a temporal reference ($t = 0$; *dotted line*), and both region- and agonist-dependent onset intervals are calculated ($n = 23$ (bourgeonal), 18 (Myrac), and 25 (PI-23472)). Along a virtual longitudinal sperm axis, Ca^{2+} signal onsets are significantly different between adjacent compartments ($p < 0.01$; note the following exceptions: (*a*) Myrac responses in the proximal flagellum, midpiece, and posterior head; (*b*) PI-23472 responses in the proximal and intermediate flagellum). In non-flagellar compartments, onset intervals are significantly shorter for Myrac responses as compared with PI-23472 and bourgeonal signals ($p < 0.01$). *B*, representative traces (F_{340}/F_{380} *versus* time) of Ca^{2+} transients recorded from different subcellular compartments (regions of interest are *color-coded*) of a single fura-2-loaded sperm challenged with PI-23472 (50 μM; 10 s; *dotted line*). On expanded coordinates (*dotted square region*; *left*), the faster response onset in the proximal and intermediate flagellum becomes apparent. *C*, Ca^{2+} extrusion in different subcellular compartments is odor-independent. Time constants (τ) of odor-specific Ca^{2+} signal decays derived from monoexponential fits (*red dashed line*; *inset*). Base Ca^{2+} levels are reconstituted significantly faster in flagellar compartments than in the acrosomal and posterior head region ($p < 0.01$; $n = 20$ (bourgeonal), 12 (Myrac), and 35 (PI-23472)). *D*, merged Ca^{2+} traces recorded from the head of the same cell in response to consecutive 10-s applications of Myrac (*blue*), PI-23472 (*black*), and bourgeonal (*red*). On expanded coordinates (*dotted square regions*), both the faster onset of the Myrac-induced signal (*left*) and the characteristic differences in response amplitudes (*right*; PI-23472 > bourgeonal > Myrac) are readily identified. *E*, stimulus identity defines characteristic response parameters. In a two-dimensional plot (amplitude *versus* rise time), response profiles derived from different sperm compartments group in odor-specific clusters. Generally, Myrac (*blue*; $n = 18$) triggers slowly rising Ca^{2+} signals of small amplitudes, whereas bourgeonal responses (*red*; $n = 21$) rise fast without reaching peak Ca^{2+} levels as induced by PI-23472 (*black*; $n = 34$). *F*, representative traces (F_{340}/F_{380} *versus* time) showing compartment-specific Ca^{2+} signals (*color-coded*) of a single spermatozoon in response to bourgeonal. The *graph* depicts the faster onset (see *A*), steeper slope (see *E*), and faster decay (see *C*) of flagellar responses as compared with Ca^{2+} signals in the acrosomal and posterior head region. *Highlighted time points 1–5* (*dotted lines*) correspond to individual *pseudocolor images* (*bottom*) illustrating relative compartment-dependent changes in Ca^{2+} concentrations (*rainbow 256 color map*; *blue*, low Ca^{2+}; *red*, high Ca^{2+}). *B*, *D*, and *F*, original traces have been mathematically smoothed using a binomial algorithm.

Together, our data indicate that all three chemosignals trigger characteristic Ca^{2+} mobilization patterns in human sperm. These are probably established by receptor/ligand-specific signaling mechanisms and might control distinct motility phenotypes.

Agonist-dependent Motility Profiles—To investigate whether stimulus-dependent sperm Ca^{2+} dynamics determine unique behaviors, we performed microcapillary accumulation assays that were complemented by CAVMA studies (16, 17) that measured single cell swimming speed and trajectories as well as flagellar beating frequency as a function of sperm exposure to different chemical concentration gradients.

As described previously (16, 17), sperm exposed to an ascending gradient of $\geq 10^{-7}$ M bourgeonal swam faster (Fig.

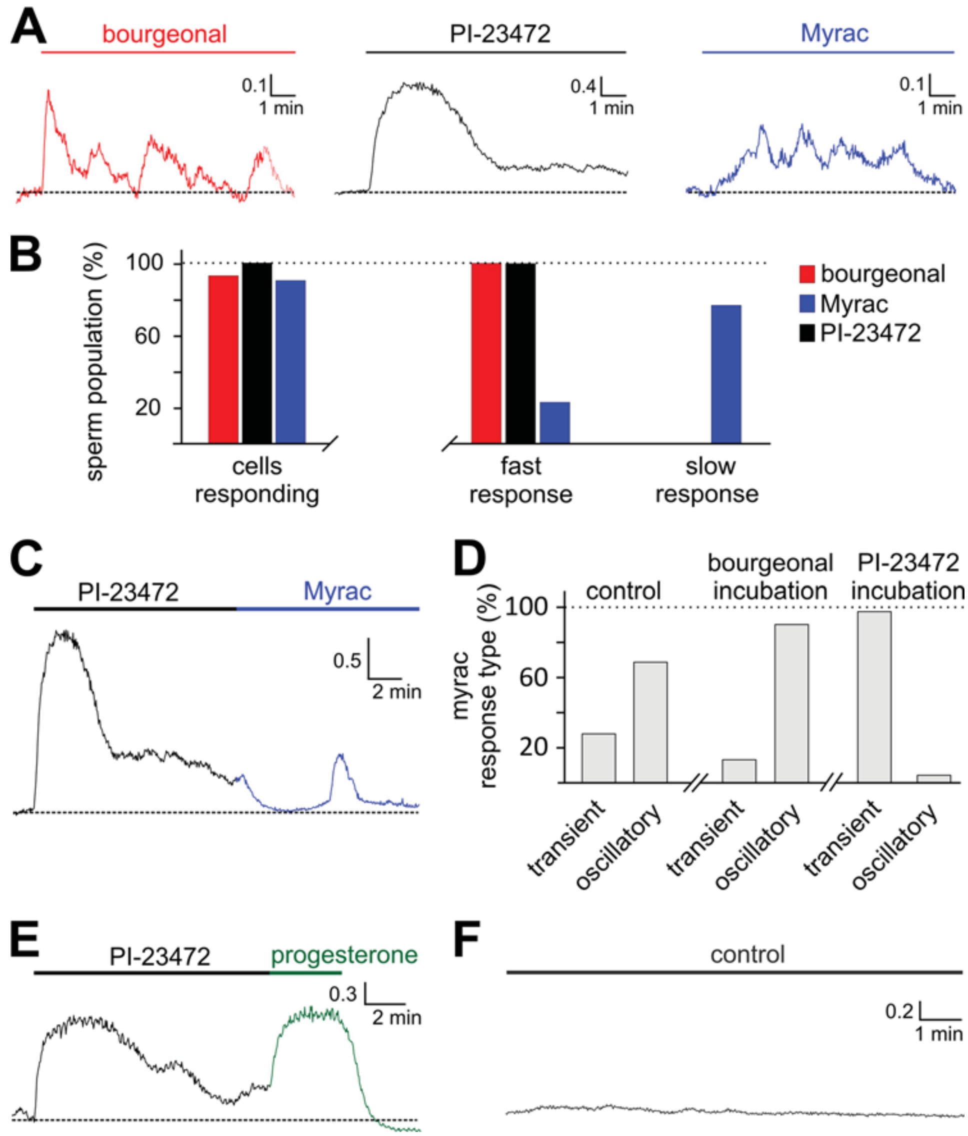

FIGURE 4. **Distinct agonist-dependent Ca^{2+} response phenotypes emerge during prolonged stimulus exposure.** *A*, Ca^{2+} signaling during constant agonist exposure (≥10 min). Shown are representative original traces (F_{340}/F_{380} *versus* time) in response to prolonged presence (*horizontal bars*) of bourgeonal (*red*), PI-23472 (*black*), and Myrac (*blue*), respectively. *B*, *bar graph* illustrating agonist-specific sperm response patterns during continuous stimulation ($n = 209$ (bourgeonal), 341 (Myrac), and 211 (PI-23472)). Bourgeonal and PI-23472 induce immediate, rapidly rising Ca^{2+} signals, whereas most Myrac-sensitive cells show a delayed, slowly developing response (see A). *C* and *D*, in a cross-adaptation paradigm, Myrac responses are affected by PI-23472 but not bourgeonal pre-exposure. Although Ca^{2+} signals triggered by prolonged Myrac and bourgeonal stimulation appear mutually independent (data not shown), prior activation by PI-23472 converts oscillatory Myrac signals to a single, transient response. *C* and *E*, representative original Ca^{2+} signals (F_{340}/F_{380} *versus* time) mediated by consecutive prolonged application (*horizontal bars*) of PI-23472 (*black*) and Myrac (*blue*) (*C*) or PI-23472 (*black*) and progesterone (*green*; $n = 120$), respectively (*E*). *F*, representative original control recording (F_{340}/F_{380} *versus* time). During constant superfusion with bath solution (control), a constant resting Ca^{2+} level is maintained ($n = 30$).

5*A*), strongly oriented with respect to the stimulus source (capillary tip) (Fig. 5*D* and supplemental Fig. S4), and accumulated inside the capillary at higher cell densities than in control experiments (Fig. 5*B*). These effects on sperm behavior were dose-dependent (supplemental Fig. S4*A*), peaked at a stimulus concentration of 10^{-6} M, and declined at concentrations of $\geq 10^{-5}$ M (data not shown), exhibiting a bell-shaped dose-response curve. In contrast, sperm exposed to an ascending gradient of Myrac or PI-23472 ($\geq 10^{-7}$ M), displayed a random orientation pattern (Fig. 5*D*). Both chemostimuli, however, significantly elevated sperm swimming speed (Fig. 5*A*). Cell densities within the capillaries were only significantly elevated in the presence of Myrac, with this increase being minor (62%) relative to bourgeonal (Fig. 5*B*; $p < 0.05$). To examine whether this Myrac-dependent cell accumulation indicates a chemotactic response (which appeared unlikely given the lack of orientation in single cell motion analysis (Fig. 5*D* and supplemental Fig. S4)), we assayed the cell density in microcapillaries when stimulus concentrations were uniform (Fig. 5*C*). In sharp contrast to bourgeonal-mediated effects, sperm accumulation in presence of uniform Myrac or PI-23472 concentrations did not significantly differ from densities observed in an ascending gradient, suggesting that the Myrac-induced increase in density is not a chemotactic but rather a chemokinetic effect (1, 7). Neither Myrac- nor PI-23472-mediated responses were affected in the presence of undecanal (Fig. 5,

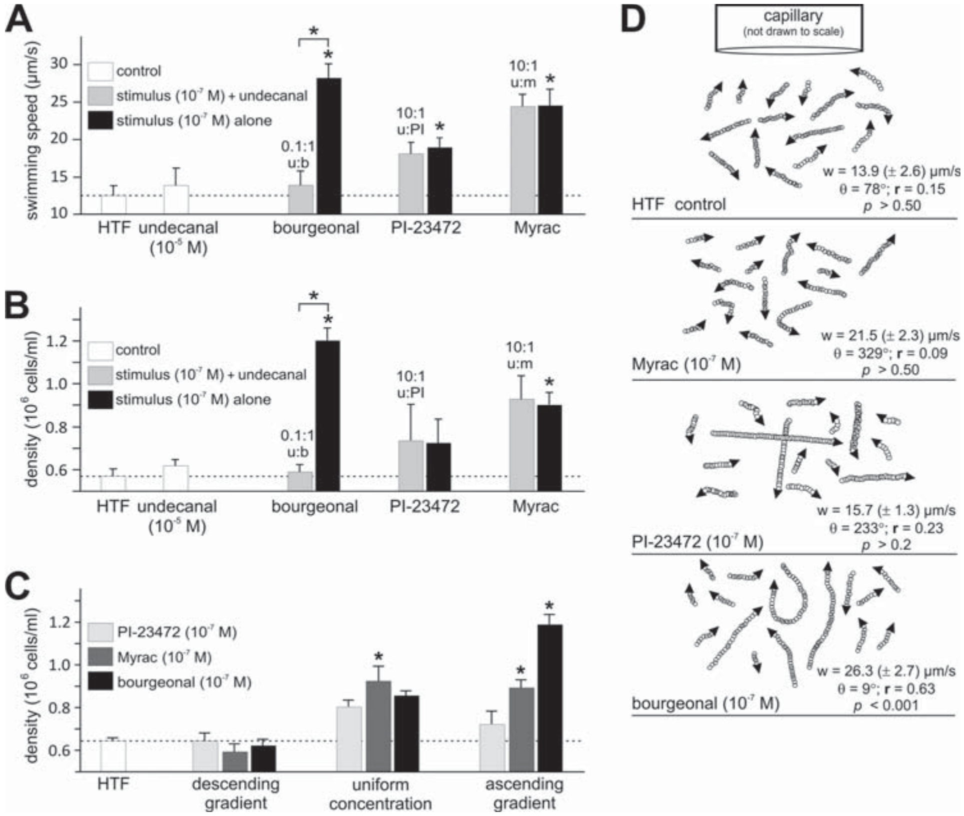

FIGURE 5. **Agonists of OR7A5 and OR4D1 boost sperm swimming speed, whereas OR1D2 signaling mediates both chemokinesis and chemotaxis.** *A* and *B*, swimming speed (*A*) and accumulation (*B*) assays of human sperm in HTF and an ascending gradient of undecanal (*u*), respectively (controls) or ascending gradients of bourgeonal (*b*), PI-23472 (*PI*), and Myrac (*m*), respectively (10^{-7} M ± equimolar undecanal). OR agonists all significantly elevate sperm velocity relative to HTF and undecanal ($p < 0.03$, all comparisons). In contrast, sperm density inside microcapillaries is significantly increased by bourgeonal and Myrac gradients but not by PI-23472 gradients. Undecanal blocks effects mediated by bourgeonal, whereas behavioral responses to PI-23472 or Myrac are unaffected. *C*, sperm accumulation in microcapillary tubes presenting an ascending gradient, uniform concentrations, or a descending chemical gradient (Myrac, bourgeonal, PI-23472 at 10^{-7} M; HTF as the control). Significantly elevated densities relative to HTF ($p < 0.05$) are observed for both bourgeonal (ascending gradient) and Myrac (ascending gradient and uniform concentration). *D*, representative randomly chosen paths of sperm in ascending gradients of Myrac, PI-23472, or bourgeonal. *Open circles* correspond to the location of sperm heads in video images captured at 30 Hz; *arrowheads* indicate directions of travel for individual cells. Analyzed motility parameters (ω, θ, r, and p) are defined as described under "Experimental Procedures." *Error bars*, S.E.

A and *B*, and supplemental Fig. S4*B*), whereas this described OR1D2 antagonist (17, 40) abolished bourgeonal-dependent behavior. Ascending gradients of undecanal alone (up to 10^{-5} M) did not induce any behavioral response (Fig. 5, *A* and B, and supplemental Fig. S4*B*). These data indicate that all three identified chemoreceptor agonists trigger distinct and stimulus-specific motility patterns in human sperm.

Previous work has shown that the population of chemotactic sperm is correlated with the percentage of capacitated cells (1). We therefore determined the capacitative state among sperm populations showing either chemosensitive (capillary recruitment) or -insensitive (residing in wells) behavior in an independent series of accumulation assays (supplemental Fig. S5*A*). Using an FITC-*Pisum sativum* agglutinin staining assay, the fraction of spontaneously acrosome-reacted sperm was similar in wells and capillaries, independent of the experimental conditions. By contrast, the proportion of sperm in which the acrosome reaction can be induced (phorbol 12-myristate 13-acetate; 5 μM; 30 min), representing sperm in a capacitated state (51), is significantly increased in cells found in capillaries after stimulus exposure. These findings suggest that the ability of a sperm not only to detect a chemotactically active stimulus but to translate this chemosignal into a meaningful behavior is somewhat dependent on attainment of the capacitative state.

Given that sperm alter flagellar motion as dictated by their environment (3), we next asked whether flagellar beating is changed when cells are exposed to ascending agonist gradients (supplemental Fig. S5, *B–D*). Frame-by-frame video motion analysis (30 Hz) revealed that both bourgeonal and Myrac induced a significant increase in the average flagellar beat frequency, whereas beating remained essentially unchanged in the presence of PI-23472 as well as undecanal (supplemental Fig. S5*B*). As observed for swimming directionality and speed (supplemental Fig. S4*A*), changes in beat frequency were dose-dependent (supplemental Fig. S5*C*). In general, both bourgeonal and Myrac elevated flagellar beat frequencies without changing the overall pattern of relatively low amplitude sinusoidal flagellar motion (supplemental Fig. S5*D*). Together, our results indicate that the chemokinetic effects of both bourgeonal and Myrac result, at least in part, from an increased flagellar beat frequency. Beating symmetry, however, remains unaltered, thus showing that neither stimulus induces hyperactivated motility.

Next, we employed laser tweezers as a non-invasive biophysical tool to examine the power at which swimming sperm

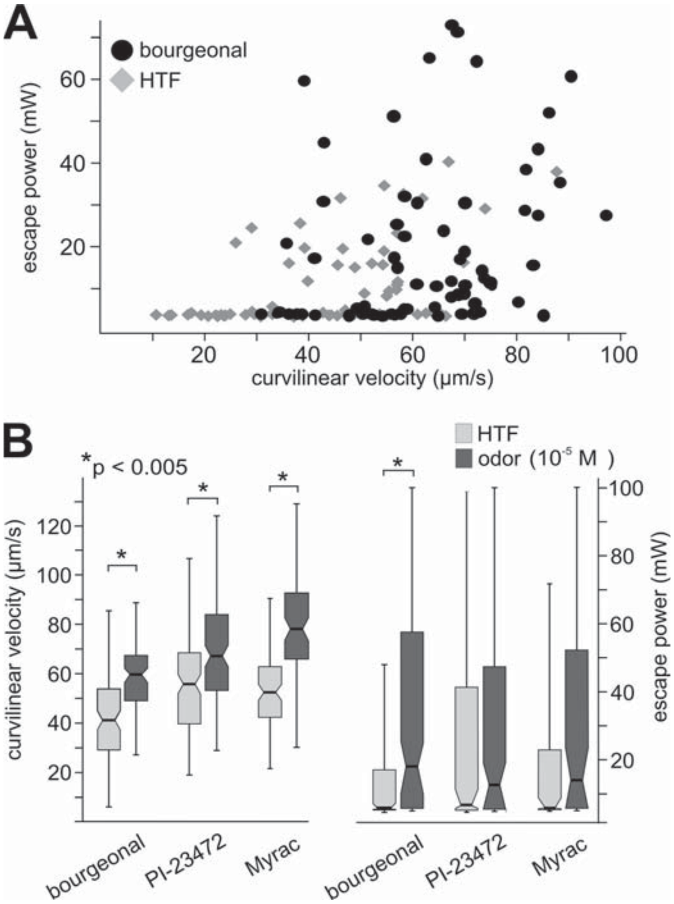

FIGURE 6. **Stimulus-evoked changes in flagellar beating, escape laser power, and curvilinear velocity.** *A*, *scatter plot* (escape power *versus* curvilinear velocity) of individual laser tweezer experiments in presence (*black filled circles*) or absence (*gray filled diamonds*) of bourgeonal. *B*, *box plot* illustrating the median values of curvilinear velocity and escape laser power of laser-trapped human sperm under control conditions (*gray*; $n = 95$ (bourgeonal), $n = 84$ (Myrac), and $n = 125$ (PI-23472)) or challenged with ascending gradients of bourgeonal, PI-23472, or Myrac (*black*; $n = 89$ (bourgeonal), $n = 64$ (Myrac), $n = 99$ (PI-23472). *Notches* in the *box* represent an estimate of the uncertainty about the median value. The box plot medians are different at the 5% significance level if their notches do not overlap. *Error bars*, S.E.

escape from an optical trap (52, 54). This value relates directly to the swimming force (in piconewtons) of individual sperm (54). RATTS allows the escape laser power for an individual cell to be measured simultaneously with its swimming speed. As predicted from CAVMA results (Fig. 5 and supplemental Fig. S4), bourgeonal, PI-23472, and Myrac significantly elevated sperm curvilinear velocity (Fig. 6*B*). This effect on swimming speed, however, was only correlated with a significant increase in escape laser power when sperm were exposed to bourgeonal (Fig. 6, *A* and *B*). Neither PI-23472 nor Myrac induced a significant increase in escape laser power. In summary, we identified three sperm chemoreceptor agonists that induce both spatially and temporally distinct and stimulus-specific Ca^{2+} mobilization patterns that correlate with individually unique behaviors.

DISCUSSION

Cells invest substantial energy to control cytosolic Ca^{2+} levels (43, 65, 66). In sperm, localized Ca^{2+} signals control flagellar beating via Ca^{2+}-sensitive axonemal motor proteins, affect sperm capacitation, and mediate the acrosome reaction, yet our conceptual understanding of how external chemosignal detection, spatiotemporally discrete Ca^{2+} signaling, and distinct behavioral responses are linked in mammalian sperm is still rudimentary. Here, we identify agonists for two orphan human ORs (OR4D1 and OR7A5) that were previously described in testis and/or mature sperm (24, 25, 32, 35). In concert with the recently identified human sperm chemoreceptor OR1D2 (17), all three recombinant receptors display broadly tuned but non-overlapping receptive fields. Analogous to OR1D2, agonists of OR4D1 and OR7A5 induce dose-dependent low threshold Ca^{2+} responses in mature human sperm. In contrast to OR-specific tuning profiles of olfactory sensory neurons, a given sperm cell is activated independently by all three agonists. We show, however, that each chemostimulus triggers a characteristic Ca^{2+} response that correlates with a stimulus-specific motility pattern. Our results thus indicate multiple stages of chemical communication between human sperm and its environment, each of which might utilize a separate receptor-ligand combination to activate an adequate context-specific sperm behavior.

Human Sperm Chemoreceptors—In most mammals, including humans, ORs constitute the largest gene superfamily, with ~400 apparently functional members in humans and ~1200 in mice (22). Despite intensive efforts, the vast majority of mammalian ORs are yet to be deorphanized (67–69). When Parmentier *et al.* (23) first proposed human OR expression in male germ cells, their finding sparked a controversial discussion about the potential function of such "ectopic" ORs. Today, numerous groups have reported mammalian OR expression on the transcript and/or protein level in both spermatogenic cells and mature sperm (16–19, 23–36). In addition, functional evidence for a physiological role of "ectopic" chemoreceptors is accumulating (17–20, 55, 71–73). In the present study, we focused on two receptors, OR4D1 and OR7A5, for which different groups had independently reported medium to high level expression in human testicular tissue and/or fertile human sperm (24, 25, 32, 35). Our quantitative PCR data suggest a high level of tissue specificity because relative expression levels in eight other human tissues (pooled high purity samples from up to 32 donors) proved negligible.

To identify specific stimuli for OR4D1 and OR7A5, we used the same experimental strategy that we had successfully employed in the past to match human OR-ligand pairs (17, 38, 55–57, 74). Given the poor OR surface expression rate typically observed in heterologous cells (47), careful evaluation of single cell Ca^{2+} responses is imperative, making this an "ultra-low throughput" assay that is neither applicable to the full repertoire of human ORs[5] nor suitable for large scale ligand screening. When successful, however, this approach has provided robust results that were later confirmed by different laboratories (39, 40, 59, 60). Recombinant OR4D1, OR7A5, and OR1D2 each respond to an apparently non-overlapping set of structurally similar low molecular weight compounds (Fig. 1, *B* and *C*). Such relatively broad yet odor subset-selective tuning profiles have also been reported for other ORs (69, 75). Thus, testicular

[5] T. Veitinger, S. Veitinger, A. Triller, K. Schwane, E. M. Neuhaus, M. Spehr, and H. Hatt, unpublished observations.

ORs appear to follow mechanistic principles similar to those of "conventional" nasal ORs. In a recent high throughput screening of 245 human ORs, including OR4D1, OR7A5, and OR1D2, against a panel of 93 structurally different odor molecules (69), a total of 10 ORs were matched to specific ligands. The three testicular ORs identified here, however, did not respond to any of the 93 test molecules, none of which bears a clear structural resemblance to bourgeonal, Myrac, or PI-23472.

For OR1D2, we could previously confirm its expression in sperm by immunocytochemistry (20). Despite several attempts, however, we failed to generate specific antibodies against both OR4D1 and OR7A5, probably because of the large size of the gene family and substantial sequence homology among its members. The testis-specific OR expression pattern we found in quantitative PCR experiments as well as both the effective Ca^{2+} mobilization and the distinct motility patterns induced in sperm by the identified OR agonists, however, suggest functional expression of OR4D1 and OR7A5 (in addition to OR1D2) in male human gametes. Activation of an individual cell by all three receptor-specific stimuli, however, suggests different transcription control mechanisms in spermatogenic cells as compared with olfactory sensory neurons in which monogenic expression of only a single type of OR is tightly controlled (22).

Chemosensory Ca^{2+} Signaling—Complex spatiotemporal Ca^{2+} dynamics orchestrate sperm motility (3). The flagellar motor, however, is not the only Ca^{2+}-dependent molecular machinery in sperm. Most vital physiological processes, such as capacitation or the acrosome reaction, are controlled by cytosolic Ca^{2+} (44, 76, 77). Therefore, functional separation of individual signaling pathways with little, if any, input integration is critical.

Using semiquantitative ratiometric Ca^{2+} imaging, we determined compartment-specific response characteristics when sperm were exposed to saturating concentrations of bourgeonal, Myrac, or PI-23472 (Fig. 3). In a given flagellar compartment, Ca^{2+} rise times were significantly different for all stimuli. *Vice versa*, considerably faster rising speeds were observed in flagellar *versus* head regions for each stimulus. In addition, PI-23472 response amplitudes were substantially increased, and the Ca^{2+} "wave" triggered by Myrac propagated significantly faster than bourgeonal- or PI-23472-mediated signals.

Despite their individually unique spatiotemporal features, Ca^{2+} responses to bourgeonal, Myrac, and PI-23472 share some commonalities. First, each characteristic response originated in proximal areas of the principal piece and showed a wave-like propagation along the cell's longitudinal axis (Fig. 3*A*). Second, for all three chemoreceptor agonists, sperm responses depend on extracellular Ca^{2+} (supplemental Fig. S2, *B* and *C*). This finding does not exclude a secondary function of Ca^{2+} storage organelles, such as the acrosome vesicle (78) or the redundant nuclear envelope (45) in response amplification/propagation, but it clearly implicates plasma membrane Ca^{2+} channels as the primary targets of all three transduction pathways. Third, Ca^{2+} clearance kinetics displayed essentially no stimulus-specific differences in a given region (Fig. 3*C*). We conclude that sperm Ca^{2+} extrusion mechanisms are functionally uncoupled from the Ca^{2+} influx machinery and, thus, stimulus-independent. Using synthetic Ca^{2+} dyes, such as fura-2, it is impossible to distinguish cytosolic from organelle-specific Ca^{2+} signals. By loading cells with membrane-permeable AM esters, some dye molecules will inevitably be hydrolyzed within, for example, the mitochondrial matrix or the acrosome. Thus, we cannot rule out a role of organelle-specific signaling in chemoreceptor Ca^{2+} cascades.

The apparent tail-to-head Ca^{2+} propagation in response to Myrac is significantly faster (~0.9 s) than recorded for both bourgeonal and PI-23472 (~3.2 s (bourgeonal) and ~2.5 s (PI-23472)) (Fig. 3*A*). The simplest explanation for this difference is that Myrac-sensitive chemoreceptors are more broadly distributed along the tail-to-head axis, whereas receptors for bourgeonal and PI-23472, respectively, are more strictly confined to the midpiece and proximal flagellum. An analog distribution pattern was recently shown for OR1D2 by immunocytochemistry (20). Pronounced antibody staining is found in the midpiece and, in a more patchy pattern, in proximal flagellar areas. Upon bourgeonal activation, β-arrestin2 mediates OR1D2 translocation from the plasma membrane. Immunofluorescent signals in the head equatorial region, however, proved essentially unaffected (20). To segregate and/or modulate head and tail Ca^{2+} signals, the sperm annulus, a membrane diffusion barrier between the principal piece and midpiece (79), and the densely packed helical array of mitochondria in the midpiece are ideally positioned to restrict lateral chemoreceptor diffusion and function as a Ca^{2+} buffer (3), respectively. This way, chemoreceptor signaling might also stimulate oxidative phosphorylation and, thus, regulate ATP generation and homeostasis.

In sperm, the identities of the signaling cascades activated downstream individual chemoreceptors remain a matter of debate. Consistent with data reported previously (16), our pharmacological experiments suggest a common pathway that involves adenylate cyclase activation. To serve distinct physiological functions, this common cascade has to split and trigger receptor-specific pathways. Such specificity could, for example, be established by expression of individual chemoreceptor types within distinct transducisomes (70). The lack of a detectable cAMP increase, however, is puzzling. Future experiments will have to address whether potential changes in cAMP occur below the detection threshold of our assay or if the drugs we used, in addition to their described function, target a yet unknown signal transduction component.

Chemosignals, Ca^{2+}, and Sperm Behavior—The control of flagellar shape and movement by Ca^{2+} is an evolutionarily conserved concept established from marine invertebrate to mammalian sperm (4, 15, 43). Flagellar (a)symmetry, amplitude, and beat frequency change as a function of Ca^{2+} mobilization, thus discretely generating straight or circular swimming paths, directed (chemotactic) turns, random (exploratory) turning, hyperactivation, or reversible motility arrest (3) according to the prevailing physicochemical conditions. Our observation that activation of different sperm chemoreceptors resulted in discrete Ca^{2+} dynamics led us to investigate whether an individual Ca^{2+} response could be linked to a distinct behavior. Microcapillary assays (comparing cell responses to an ascending chemical concentration gradient, a descending gradient, and a uniform chemical concentration field; Fig. 5) faithfully measure sperm accumulation and allow the distinction between positive or negative chemotaxis, chemokinesis, and trapping (1). Single cell motion analysis and path tracking (Fig. 5*D* and supplemental Figs. S4 and S5) in an ascending three-dimensional chemical gradient capture a complementary "snapshot" of the mechanisms underlying cell accumulation patterns and, thus, provide information on directionality, swimming speed, and flagellar waveform/beat frequency. In addition, laser tweezers provide another non-invasive tool to examine swimming force by determining the laser power required for individual sperm cells to escape from an optical trap. When used with RATTS, sperm curvilinear velocity can be correlated with the escape laser power (52). Together, each tool in this analytical "package" adds valuable information on chemoreceptor-mediated sperm behavior. None of the assays, however, measures percentages of chemosensitive cells because each bioassay is time-critical (*e.g.* prior recruitment of chemotactic sperm during gradient establishment). In fact, we expect the actual population of chemotactic cells to correlate closely with the fraction of sperm that has adopted the capacitated state at any given point in time (*i.e.* ~10–15% (supplemental Fig. S5*A*)). As might be expected from the observed stimulus-specific Ca^{2+} dynamics, distinct behavioral "output" patterns were generated by bourgeonal, Myrac, and PI-23472, respectively. Among the three chemoreceptor agonists, only bourgeonal functions as a chemoattractant. All three stimuli increase flagellar beating frequency and thus velocity, but a significant increase in propulsion force only occurs in response to bourgeonal. None of the stimuli caused asymmetric "whiplike" beating, indicating that neither agonist caused hyperactivation.

How do these findings complement our current concepts of sperm navigation in the female reproductive tract? First, our data strengthen the notion that sperm guidance might be much more elaborate than originally thought (1). Second, we propose that individual chemosensory receptors and signaling pathways are utilized at different prefusion stages during a sperm's journey.

The chemoreceptor agonists identified in this study all represent synthetic compounds. Thus, a major effort in future research will have to be directed toward identifying both the chemical nature of the endogenous "genuine" ligands of sperm chemoreceptors and their individual secretion sources.

Acknowledgments—We greatly appreciate the gifts of bourgeonal samples from Dr. Charles Sell (Givaudan, Ashford, UK) and both Myrac and PI-23472 samples from Dr. Johannes Panten (Symrise, Holzminden, Germany). We are grateful to Michael Eisenbach and Leah Armon (Weizmann Institute of Science, Rehovot, Israel) for fruitful discussions. We thank Corinna Engelhardt, Harald Bartel, Susanne Lipartowski, and Jasmin Gerkrath for excellent technical assistance.

REFERENCES

1. Eisenbach, M., and Giojalas, L. C. (2006) *Nat. Rev. Mol. Cell. Biol.* **7,** 276–285
2. Bahat, A., Tur-Kaspa, I., Gakamsky, A., Giojalas, L. C., Breitbart, H., and Eisenbach, M. (2003) *Nat. Med.* **9,** 149–150
3. Publicover, S., Harper, C. V., and Barratt, C. (2007) *Nat. Cell. Biol.* **9,** 235–242
4. Navarro, B., Kirichok, Y., Chung, J. J., and Clapham, D. E. (2008) *Int. J. Dev. Biol.* **52,** 607–613
5. Darszon, A., Treviño, C. L., Wood, C., Galindo, B., Rodríguez-Miranda, E., Acevedo, J. J., Hernandez-González, E. O., Beltrán, C., Martínez-López, P., and Nishigaki, T. (2007) *Soc. Reprod. Fertil. Suppl.* **65,** 229–244
6. Eisenbach, M., and Tur-Kaspa, I. (1999) *BioEssays* **21,** 203–210
7. Kaupp, U. B., Kashikar, N. D., and Weyand, I. (2008) *Annu. Rev. Physiol.* **70,** 93–117
8. Oren-Benaroya, R., Orvieto, R., Gakamsky, A., Pinchasov, M., and Eisenbach, M. (2008) *Hum. Reprod.* **23,** 2339–2345
9. Bedford, J. M., and Kim, H. H. (1993) *J. Exp. Zool.* **265,** 321–328
10. Teves, M. E., Guidobaldi, H. A., Uñates, D. R., Sanchez, R., Miska, W., Publicover, S. J., Morales Garcia, A. A., and Giojalas, L. C. (2009) *PLoS One* **4,** e8211
11. Sun, F., Bahat, A., Gakamsky, A., Girsh, E., Katz, N., Giojalas, L. C., Tur-Kaspa, I., and Eisenbach, M. (2005) *Hum. Reprod.* **20,** 761–767
12. Spehr, M., Schwane, K., Riffell, J. A., Zimmer, R. K., and Hatt, H. (2006) *Mol. Cell. Endocrinol.* **250,** 128–136
13. Kaupp, U. B., Solzin, J., Hildebrand, E., Brown, J. E., Helbig, A., Hagen, V., Beyermann, M., Pampaloni, F., and Weyand, I. (2003) *Nat. Cell. Biol.* **5,** 109–117
14. Strünker, T., Weyand, I., Bönigk, W., Van, Q., Loogen, A., Brown, J. E., Kashikar, N., Hagen, V., Krause, E., and Kaupp, U. B. (2006) *Nat. Cell. Biol.* **8,** 1149–1154
15. Wood, C. D., Nishigaki, T., Furuta, T., Baba, S. A., and Darszon, A. (2005) *J. Cell. Biol.* **169,** 725–731
16. Spehr, M., Schwane, K., Riffell, J. A., Barbour, J., Zimmer, R. K., Neuhaus, E. M., and Hatt, H. (2004) *J. Biol. Chem.* **279,** 40194–40203
17. Spehr, M., Gisselmann, G., Poplawski, A., Riffell, J. A., Wetzel, C. H., Zimmer, R. K., and Hatt, H. (2003) *Science* **299,** 2054–2058
18. Fukuda, N., and Touhara, K. (2006) *Genes Cells* **11,** 71–81
19. Fukuda, N., Yomogida, K., Okabe, M., and Touhara, K. (2004) *J. Cell. Sci.* **117,** 5835–5845
20. Neuhaus, E. M., Mashukova, A., Barbour, J., Wolters, D., and Hatt, H. (2006) *J. Cell. Sci.* **119,** 3047–3056
21. Buck, L., and Axel, R. (1991) *Cell* **65,** 175–187
22. Mombaerts, P. (2004) *Nat. Rev. Neurosci.* **5,** 263–278
23. Parmentier, M., Libert, F., Schurmans, S., Schiffmann, S., Lefort, A., Eggerickx, D., Ledent, C., Mollereau, C., Gérard, C., and Perret, J. (1992) *Nature* **355,** 453–455
24. Vanderhaeghen, P., Schurmans, S., Vassart, G., and Parmentier, M. (1997) *Biochem. Biophys. Res. Commun.* **237,** 283–287
25. Vanderhaeghen, P., Schurmans, S., Vassart, G., and Parmentier, M. (1997) *Genomics* **39,** 239–246
26. Vanderhaeghen, P., Schurmans, S., Vassart, G., and Parmentier, M. (1993) *J. Cell. Biol.* **123,** 1441–1452
27. Walensky, L. D., Roskams, A. J., Lefkowitz, R. J., Snyder, S. H., and Ronnett, G. V. (1995) *Mol. Med.* **1,** 130–141
28. Zhang, X., De la Cruz, O., Pinto, J. M., Nicolae, D., Firestein, S., and Gilad, Y. (2007) *Genome Biol.* **8,** R86
29. Zhang, X., Rogers, M., Tian, H., Zhang, X., Zou, D. J., Liu, J., Ma, M., Shepherd, G. M., and Firestein, S. J. (2004) *Proc. Natl. Acad. Sci. U.S.A.* **101,** 14168–14173
30. Goto, T., Salpekar, A., and Monk, M. (2001) *Mol. Hum. Reprod.* **7,** 553–558
31. Baker, M. A., Hetherington, L., Reeves, G. M., and Aitken, R. J. (2008) *Proteomics* **8,** 1720–1730
32. Feldmesser, E., Olender, T., Khen, M., Yanai, I., Ophir, R., and Lancet, D. (2006) *BMC Genomics* **7,** 121
33. Asai, H., Kasai, H., Matsuda, Y., Yamazaki, N., Nagawa, F., Sakano, H., and Tsuboi, A. (1996) *Biochem. Biophys. Res. Commun.* **221,** 240–247
34. Schultz, N., Hamra, F. K., and Garbers, D. L. (2003) *Proc. Natl. Acad. Sci. U.S.A.* **100,** 12201–12206
35. Platts, A. E., Dix, D. J., Chemes, H. E., Thompson, K. E., Goodrich, R., Rockett, J. C., Rawe, V. Y., Quintana, S., Diamond, M. P., Strader, L. F., and Krawetz, S. A. (2007) *Hum. Mol. Genet.* **16,** 763–773
36. De la Cruz, O., Blekhman, R., Zhang, X., Nicolae, D., Firestein, S., and

Gilad, Y. (2009) *Mol. Biol. Evol.* **26,** 491–494
37. Branscomb, A., Seger, J., and White, R. L. (2000) *Genetics* **156,** 785–797
38. Triller, A., Boulden, E. A., Churchill, A., Hatt, H., Englund, J., Spehr, M., and Sell, C. S. (2008) *Chem. Biodivers.* **5,** 862–886
39. Cook, B. L., Steuerwald, D., Kaiser, L., Graveland-Bikker, J., Vanberghem, M., Berke, A. P., Herlihy, K., Pick, H., Vogel, H., and Zhang, S. (2009) *Proc. Natl. Acad. Sci. U.S.A.* **106,** 11925–11930
40. Kaiser, L., Graveland-Bikker, J., Steuerwald, D., Vanberghem, M., Herlihy, K., and Zhang, S. (2008) *Proc. Natl. Acad. Sci. U.S.A.* **105,** 15726–15731
41. Gakamsky, A., Armon, L., and Eisenbach, M. (2009) *Hum. Reprod.* **24,** 1152–1163
42. Berridge, M. J., Lipp, P., and Bootman, M. D. (2000) *Science* **287,** 1604–1605
43. Clapham, D. E. (2007) *Cell* **131,** 1047–1058
44. Bedu-Addo, K., Costello, S., Harper, C., Machado-Oliveira, G., Lefievre, L., Ford, C., Barratt, C., and Publicover, S. (2008) *Int. J. Dev. Biol.* **52,** 615–626
45. Ho, H. C., and Suarez, S. S. (2003) *Biol. Reprod.* **68,** 1590–1596
46. Rivière, S., Challet, L., Fluegge, D., Spehr, M., and Rodriguez, I. (2009) *Nature* **459,** 574–577
47. Saito, H., Kubota, M., Roberts, R. W., Chi, Q., and Matsunami, H. (2004) *Cell* **119,** 679–691
48. Toffle, R. C., Nagel, T. C., Tagatz, G. E., Phansey, S. A., Okagaki, T., and Wavrin, C. A. (1985) *Fertil. Steril.* **43,** 743–747
49. Riffell, J. A., Krug, P. J., and Zimmer, R. K. (2002) *J. Exp. Biol.* **205,** 1439–1450
50. Gee, C. C., and Zimmer-Faust, R. K. (1997) *J. Exp. Biol.* **200,** 3185–3192
51. Breitbart, H., and Naor, Z. (1999) *Rev. Reprod.* **4,** 151–159
52. Nascimento, J. M., Botvinick, E. L., Shi, L. Z., Durrant, B., and Berns, M. W. (2006) *J. Biomed. Opt.* **11,** 044001
53. Shi, L. Z., Nascimento, J. M., Chandsawangbhuwana, C., Botvinick, E. L., and Berns, M. W. (2008) *Biomed. Microdevices* **10,** 573–583
54. Nascimento, J. M., Shi, L. Z., Meyers, S., Gagneux, P., Loskutoff, N. M., Botvinick, E. L., and Berns, M. W. (2008) *J. R. Soc. Interface* **5,** 297–302
55. Neuhaus, E. M., Zhang, W., Gelis, L., Deng, Y., Noldus, J., and Hatt, H. (2009) *J. Biol. Chem.* **284,** 16218–16225
56. Neuhaus, E. M., Mashukova, A., Zhang, W., Barbour, J., and Hatt, H. (2006) *Chem. Senses* **31,** 445–452
57. Wetzel, C. H., Oles, M., Wellerdieck, C., Kuczkowiak, M., Gisselmann, G., and Hatt, H. (1999) *J. Neurosci.* **19,** 7426–7433
58. Malnic, B., Hirono, J., Sato, T., and Buck, L. B. (1999) *Cell* **96,** 713–723
59. Marrakchi, M., Vidic, J., Jaffrezic-Renault, N., Martelet, C., and Pajot-Augy, E. (2007) *Eur. Biophys. J.* **36,** 1015–1018
60. Jacquier, V., Pick, H., and Vogel, H. (2006) *J. Neurochem.* **97,** 537–544
61. Jordt, S. E., Bautista, D. M., Chuang, H. H., McKemy, D. D., Zygmunt, P. M., Högestätt, E. D., Meng, I. D., and Julius, D. (2004) *Nature* **427,** 260–265
62. Hess, K. C., Jones, B. H., Marquez, B., Chen, Y., Ord, T. S., Kamenetsky, M., Miyamoto, C., Zippin, J. H., Kopf, G. S., Suarez, S. S., Levin, L. R., Williams, C. J., Buck, J., and Moss, S. B. (2005) *Dev. Cell.* **9,** 249–259
63. Grynkiewicz, G., Poenie, M., and Tsien, R. Y. (1985) *J. Biol. Chem.* **260,** 3440–3450
64. Takahashi, A., Camacho, P., Lechleiter, J. D., and Herman, B. (1999) *Physiol. Rev.* **79,** 1089–1125
65. Berridge, M. J. (2005) *Annu. Rev. Physiol.* **67,** 1–21
66. Berridge, M. J., Bootman, M. D., and Roderick, H. L. (2003) *Nat. Rev. Mol. Cell. Biol.* **4,** 517–529
67. Kaupp, U. B. (2010) *Nat. Rev. Neurosci.* **11,** 188–200
68. Spehr, M., and Munger, S. D. (2009) *J. Neurochem.* **109,** 1570–1583
69. Saito, H., Chi, Q., Zhuang, H., Matsunami, H., and Mainland, J. D. (2009) *Sci. Signal.* **2,** ra9
70. Castillo, K., Restrepo, D., and Bacigalupo, J. (2010) *Eur. J. Neurosci.* **32,** 932–938
71. Griffin, C. A., Kafadar, K. A., and Pavlath, G. K. (2009) *Dev. Cell* **17,** 649–661
72. Braun, T., Voland, P., Kunz, L., Prinz, C., and Gratzl, M. (2007) *Gastroenterology* **132,** 1890–1901
73. Margolskee, R. F., Dyer, J., Kokrashvili, Z., Salmon, K. S., Ilegems, E., Daly, K., Maillet, E. L., Ninomiya, Y., Mosinger, B., and Shirazi-Beechey, S. P. (2007) *Proc. Natl. Acad. Sci. U.S.A.* **104,** 15075–15080
74. Doszczak, L., Kraft, P., Weber, H. P., Bertermann, R., Triller, A., Hatt, H., and Tacke, R. (2007) *Angew. Chem. Int. Ed. Engl.* **46,** 3367–3371
75. Oka, Y., Omura, M., Kataoka, H., and Touhara, K. (2004) *EMBO. J.* **23,** 120–126
76. Jimenez-Gonzalez, C., Michelangeli, F., Harper, C. V., Barratt, C. L., and Publicover, S. J. (2006) *Hum. Reprod. Update* **12,** 253–267
77. Publicover, S. J., Giojalas, L. C., Teves, M. E., de Oliveira, G. S., Garcia, A. A., Barratt, C. L., and Harper, C. V. (2008) *Front. Biosci.* **13,** 5623–5637
78. Costello, S., Michelangeli, F., Nash, K., Lefievre, L., Morris, J., Machado-Oliveira, G., Barratt, C., Kirkman-Brown, J., and Publicover, S. (2009) *Reproduction* **138,** 425–437
79. Kwitny, S., Klaus, A. V., and Hunnicutt, G. R. (2010) *Biol. Reprod.* **82,** 669–678

Veitinger *et al.*, supplemental Fig S1

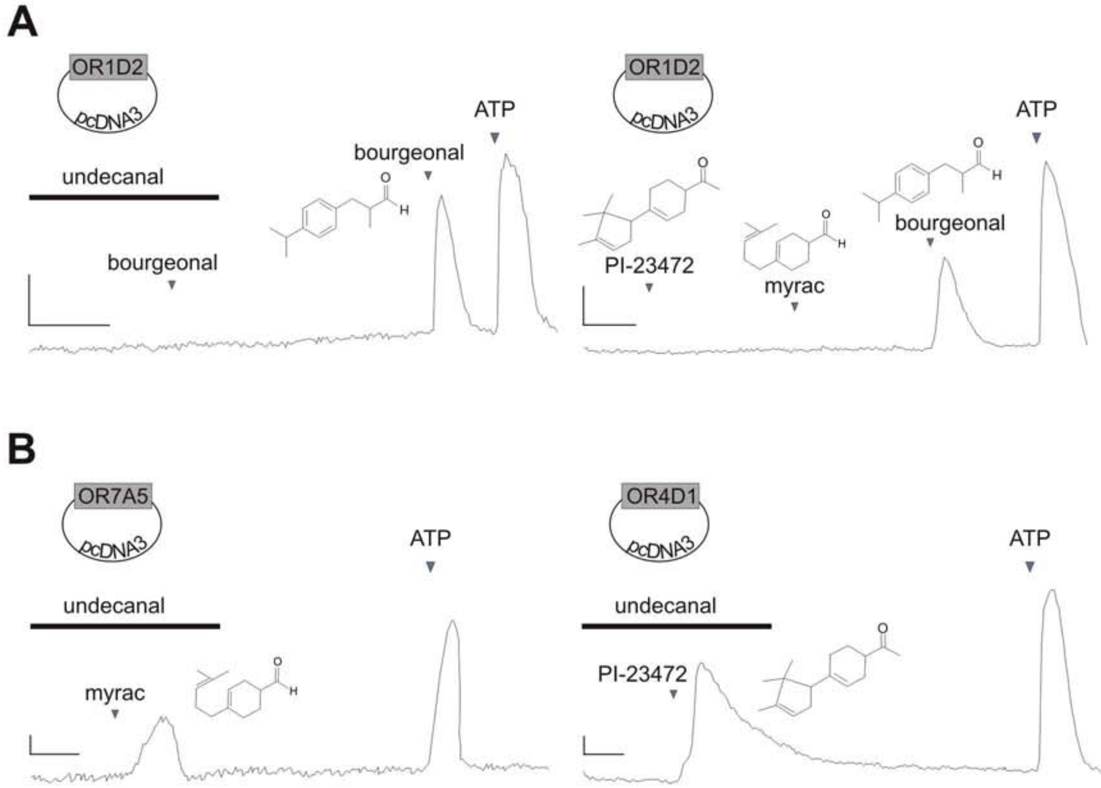

Fig. S1. Representative original Ca^{2+} recordings from agonist-sensitive HEK293 cells expressing OR1D2, OR7A5, or OR4D1, respectively. *A.* OR1D2 is neither activated by PI-23472 nor myrac, but responds to bourgeonal in absence of undecanal (50 μM). *B.* Activation of OR7A5 and OR4D1 is unaffected by undecanal incubation (black horizontal bar). Scale bars: $f_{340}/f_{380} = 0.1$ (vertical); time = 30 s (horizontal).

Veitinger *et al.*, supplemental Fig. S2

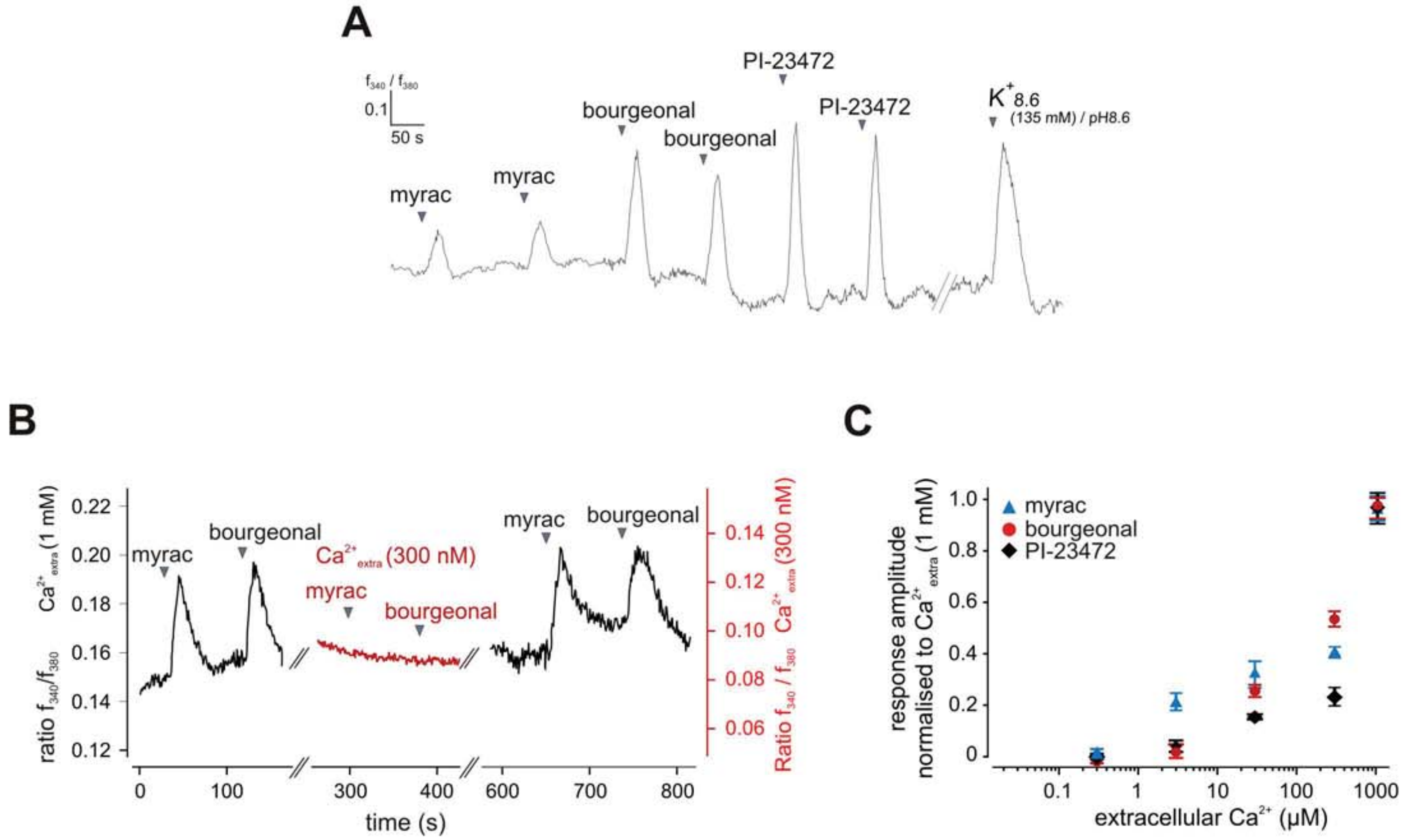

<u>Fig. S2.</u> *A*. Representative original trace (f_{340}/f_{380} *versus* time) illustrating Ca^{2+} signals of a single spermatozoon in response to repetitive odor stimulation (50 µM; 10 s). *B & C*. Odor-triggered Ca^{2+} responses are dependent on extracellular Ca^{2+}. *B*. Representative original Ca^{2+} signals recorded from the head and midpiece regions of a single fura-2 loaded cell. The integrated fluorescence ratio f_{340}/f_{380} is shown as a function of time. Brief focal application of bourgeonal and myrac (50 µM; 10 s) triggers transient increases in cytosolic Ca^{2+} that are abolished when sperm are incubated in low Ca^{2+} medium (red; EGTA-buffered; extracellular Ca^{2+} = 300 nM). *C*. Odor response amplitude is directly correlated to the extracellular Ca^{2+} concentration. Semi-logarithmic plot of agonist-specific normalized Ca^{2+} signal amplitudes (myrac (blue; $n \geq 69$), bourgeonal (red; $n \geq 53$), PI-23472 (black; $n \geq 90$)) *versus* increasing extracellular Ca^{2+} concentrations.

Veitinger *et al*., supplemental Fig. S3

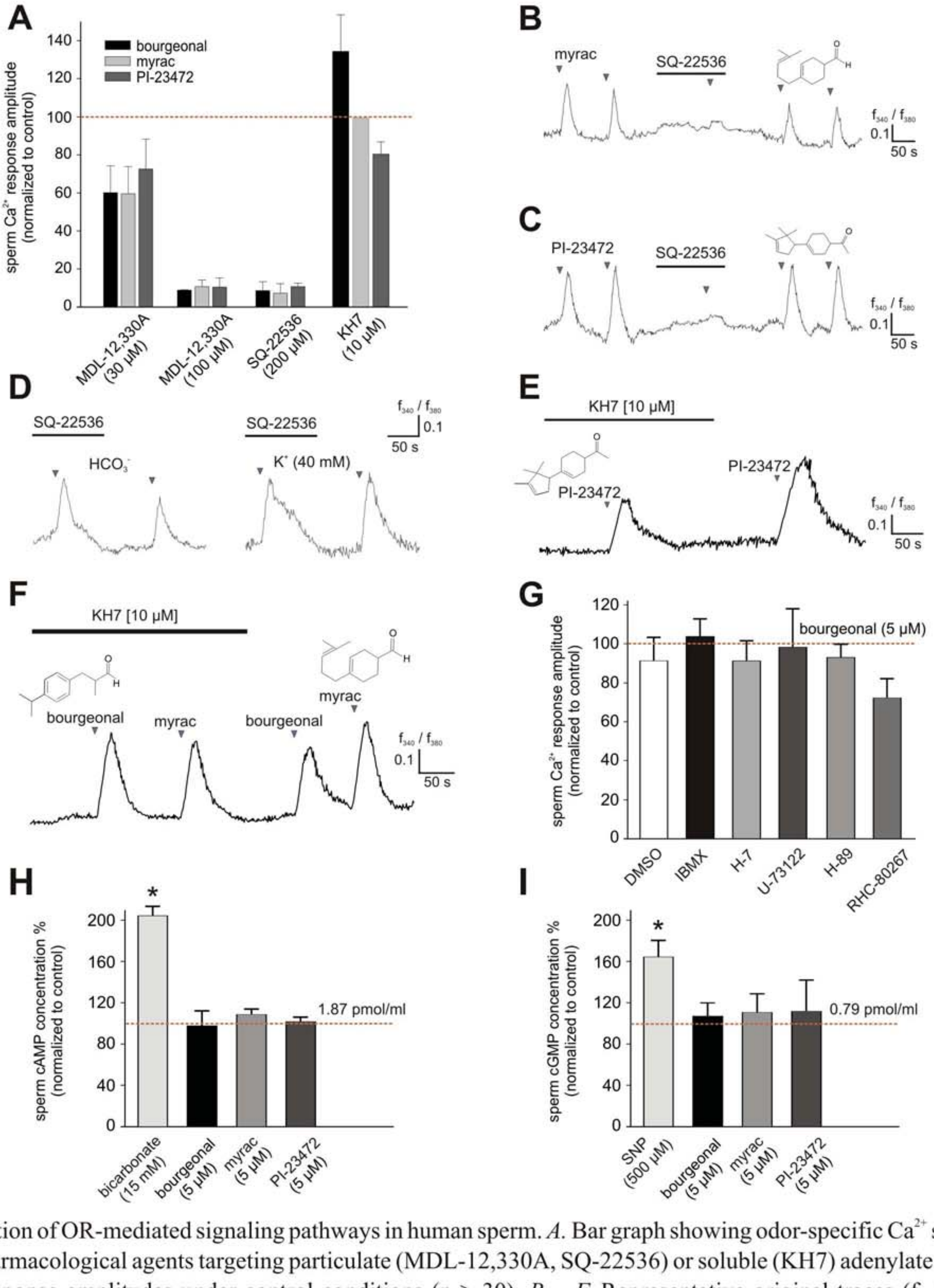

Fig. S3. Investigation of OR-mediated signaling pathways in human sperm. *A.* Bar graph showing odor-specific Ca^{2+} signal amplitudes in presence of pharmacological agents targeting particulate (MDL-12,330A, SQ-22536) or soluble (KH7) adenylate cyclase. Data are normalized to response amplitudes under control conditions ($n > 30$). *B. - F.* Representative original traces (f_{340}/f_{380} *versus* time) illustrating Ca^{2+} signals of single spermatozoa in response to repetitive odor stimulation in presence (black horizontal bars) or absence of different adenylate cyclase inhibitors. *G.* Pharmacological profile of bourgeonal-induced Ca^{2+} signals in human sperm as assessed by population response imaging in microtiter plates ($n = 11$). Peak ratiometric Ca^{2+} signals (f_{340}/f_{380}) in presence of various drugs (name / inhibited protein: IBMX / phosphodiesterases; H-7 / protein kinase C; U-73122 / phospholipase C; H-89 / protein kinase A; RHC-80267 / DAG lipase) are normalized to bourgeonal-induced response amplitudes (5 µM; dotted horizontal line). 0.1 % DMSO is tested as solvent control. None of the drugs significantly affected OR1D2-mediated Ca^{2+} signals. *H. & I.* ELISA-based quantitative cyclic nucleotide production assays (cAMP (H), cGMP (I)). Human sperm are challenged with bicarbonate (activator of soluble adenylate cyclase), SNP (NO donor; activator of guanylyl cyclase), bourgeonal, myrac, and PI-23472. Intracellular cAMP / cGMP concentration are normalized to results obtained without stimulation (dotted horizontal line).

Veitinger *et al*., supplemental Fig. S4

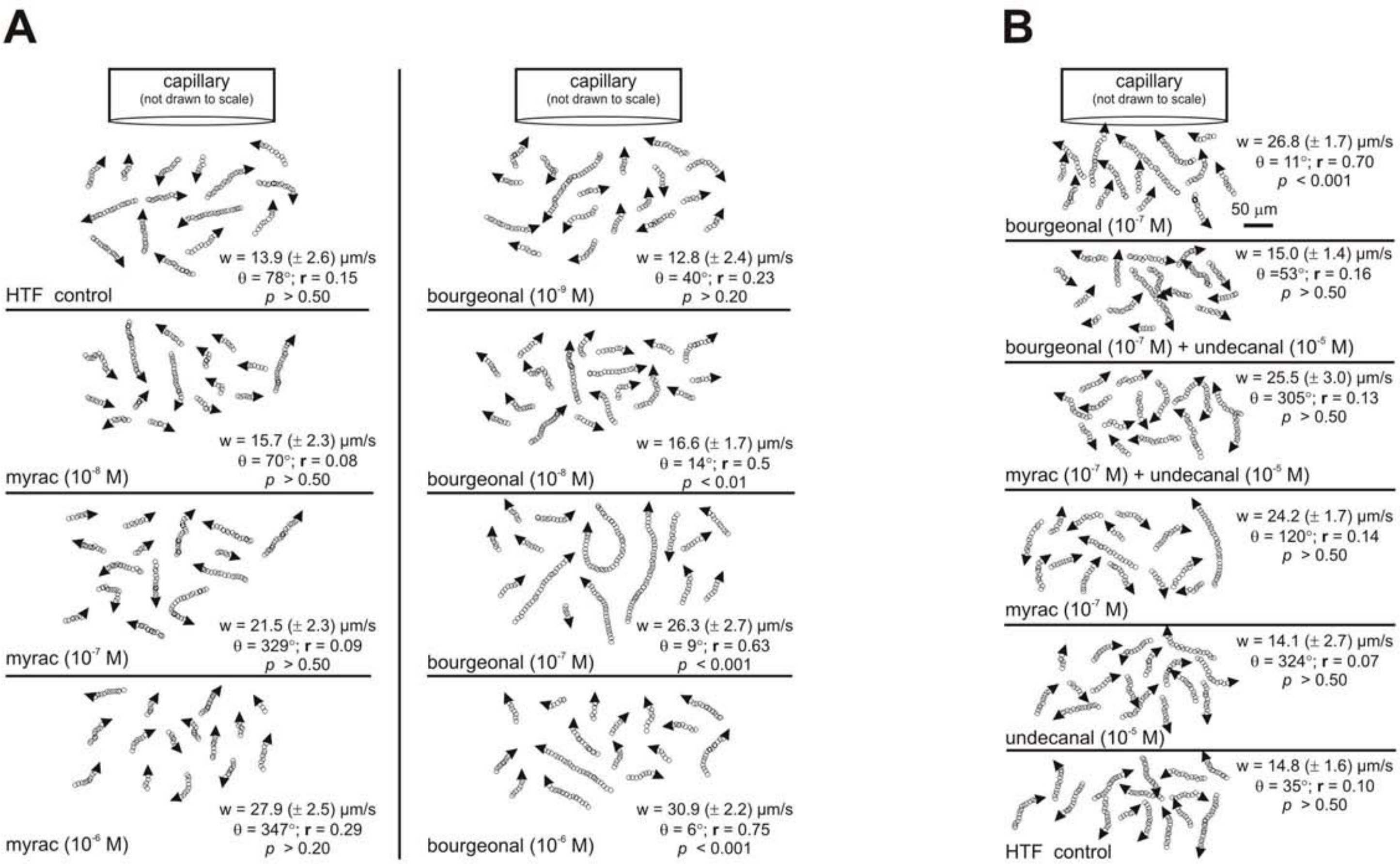

Fig. S4. Representative randomly chosen paths of sperm in ascending gradients of undecanal myrac (± undecanal) or bourgeonal (± undecanal) at different concentrations. Open circles correspond to the location of sperm heads in video images captured at 30 Hz; arrowheads indicate directions of travel for individual cells. Analyzed motility parameters (ω, θ, r, *p*) are defined as described (see Experimental Procedures).

Veitinger *et al*., supplemental Fig. S5

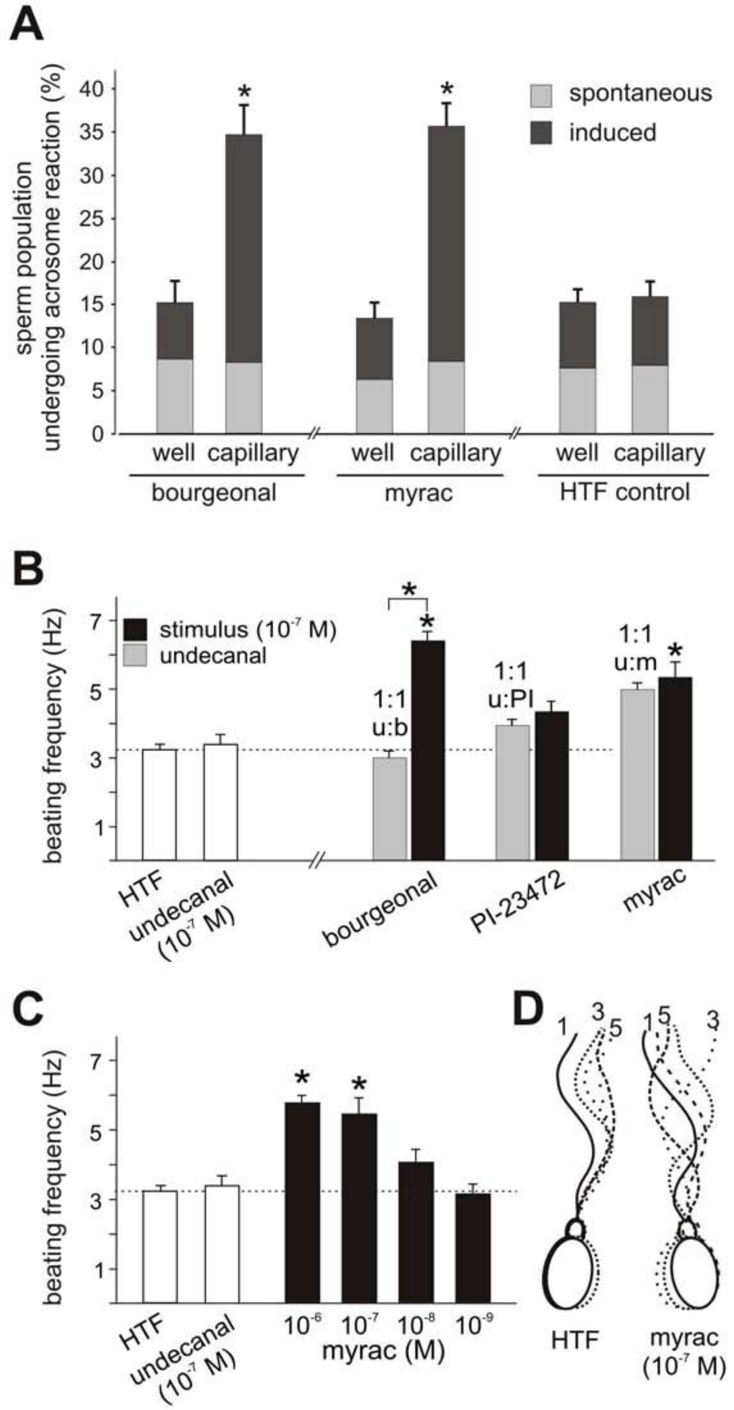

Fig. S5. *A*. Bar chart illustrating the percentage of capacitated cells among odor-sensitive *versus* -insensitive sperm populations. Presenting ascending odor gradients in at least 15 independent behavioural assays, cells that recruited to microcapillaries as compared to sperm in wells were probed for their ability to undergo an acrosome reaction, either spontaneous (grey) or induced (black). Asterisks denote a significant difference from HTF control (one-way ANOVA and post-hoc Fisher's test: F7, 163 = 6.96, $p < 0.001$). *B*. Bar chart displaying sperm flagellar beating frequency in response to ascending gradients of bourgeonal, PI-23472, or myrac (10^{-7} M) in absence (black) or presence (grey) of equimolar undecanal. Asterisks indicate significant differences between a) odor stimulation and control (HTF) or b) an odorant alone and the undecanal-odorant mixture (one-way ANOVA, Scheffé test: $p < 0.05$). *C*. Dose dependence of increased flagellar beating in response to myrac (10^{-9} - 10^{-6} M; left). *D*. Original representative flagellar waveform traces of sperm exposed to HTF and myrac. For sperm exposed to myrac, one full beat occupied six frames. In contrast, sperm in the HTF-control solution completed a full beat cycle within 11 frames.

Veitinger *et al.*, Supplemental Table S1

target	*forward primer 5´-3´*	*probe 5´-3´*	*reverse primer 5´-3´*
OR1D2	TGGAGGCAACCAGAGTGAAG	(FAM)TCAGAGTTCCTTCTCC TGGGGATGTC(TAMRA)	GCTGCTGCTCAGGACTCTCT
OR2M4	TAGTGCTTGCAGCTGTCCTG	(FAM)TCTTACTGCAGCTCTC TGGAAATTCATCA(TAMRA)	GGCAGCAACATCACAGAAAA
OR4D1	CCACAGAACACCACACAGGT	(FAM)TGTCCTCTTAGGGTTT TCACAGACCCA(TAMRA)	GAAGGAACAGGAATTTCTGGAG
OR5D16	GGAACTGCAAATTCCCCTCT	(FAM)TTGTATTTCTGGCAGT CTACGGCTTCA(TAMRA)	TCCCAAGATTCCCTACCACA
OR7A5	CCTGTGCATCTCACCTCTCA	(FAM)TTTATGGTGCAATCCT AGGGGTGTACC(TAMRA)	CGGGTGGCAGCAGAACTA
β-actin	CGTCTTCCCCTCCATCGT	(FAM)AGGCACCAGGGCGTG ATGGT(TAMRA)	GGAATCCTTCTGACCCATGC